Chapter 5. Nanostructures Technology, Research and Applications

Academic and Research Staff

Professor Henry I. Smith, Dr. Mark L. Schattenburg, Dr. Anne Pepin, Richard J. Aucoin, James M. Carter, Robert C. Fleming, Euclid E. Moon, Scott E. Silverman

Visiting Scientists and Research Affiliates

Patrick N. Everett

Graduate Students

David Berman, Martin Burkhardt, David J. Carter, Jay N. Damask, Juan Ferrera, James S. Foresi, Andrea E. Franke, Marc Hill, Keith M. Jackson, Michael H. Lim, Mitchell W. Meinhold, Thomas E. Murphy, Timothy A. Savas, Satyen Shah, Ilia Sokolinski, Vincent V. Wong, Isabel Y. Yang, Anto Yasaka

Technical and Support Staff

Mark K. Mondol, Edward Murphy, Jeanne M. Porter, Margaret A. Flaherty, Lisa Zeidenberg

5.1 Nanostructures Laboratory

The Nanostructures Laboratory (NSL) at MIT develops techniques for fabricating surface structures with feature sizes in the range from nanometers to micrometers and uses these structures in a variety of research projects. The NSL includes facilities for lithography (photo, interferometric, electron beam, ion beam, and x-ray), etching (chemical, plasma and reactive-ion), liftoff, electroplating, sputter deposition and e-beam evaporation. Much of the equipment, and nearly all of the methods, utilized in the NSL are developed in house. Generally, commercial processing equipment designed for the semiconductor industry cannot achieve the resolution needed for nanofabrication, is inordinately expensive, and lacks the required flexibility.

The research projects within the NSL fall into three major categories: (1) development of submicron and nanometer fabrication technology; (2) short-channel semiconductor devices, quantum-effect electronics, and optoelectronics; (3) periodic structures for x-ray optics, spectroscopy, atomic interferometry, and nanometer metrology.

5.2 Scanning Electron Beam Lithography

Sponsors

Joint Services Electronics Program
Grant DAAH04-95-1-0038

Semiconductor Research Corporation
Contract 95-LJ-550

Project Staff

Scott E. Silverman, Juan Ferrera, Professor Henry I. Smith

Figure 1 is a photograph of the scanning-electron-beam lithography (SEBL) system (VS-PL) located in Room 38-185. This instrument was obtained as a donation from IBM Corporation in November 1993. It is an experimental system based on many years of IBM technology development in SEBL. In 1994, a digital pattern generator was implemented, based on a commercial high performance array processor, which utilizes dual RISC processors. In 1995, the capabilities of the pattern generator hardware were augmented. New shape primitives were incorporated into its software. Also, it is now possible to expose large mask designs composed of many stitched fields. Complementary to the pattern generator development was the implementation of conversion software, which allows a CAD data file to be fractured and translated prior to exposure by the electron-beam tool.

The VS-PL system is the cornerstone of a facility for high performance electron-beam lithography. The goals of the facility are to provide the MIT research community with an in-house SEBL capability for writing directly on experimental device substrates; to advance the state-of-the-art in SEBL, particularly with regard to pattern placement accuracy and long-range spatial-phase coherence; and

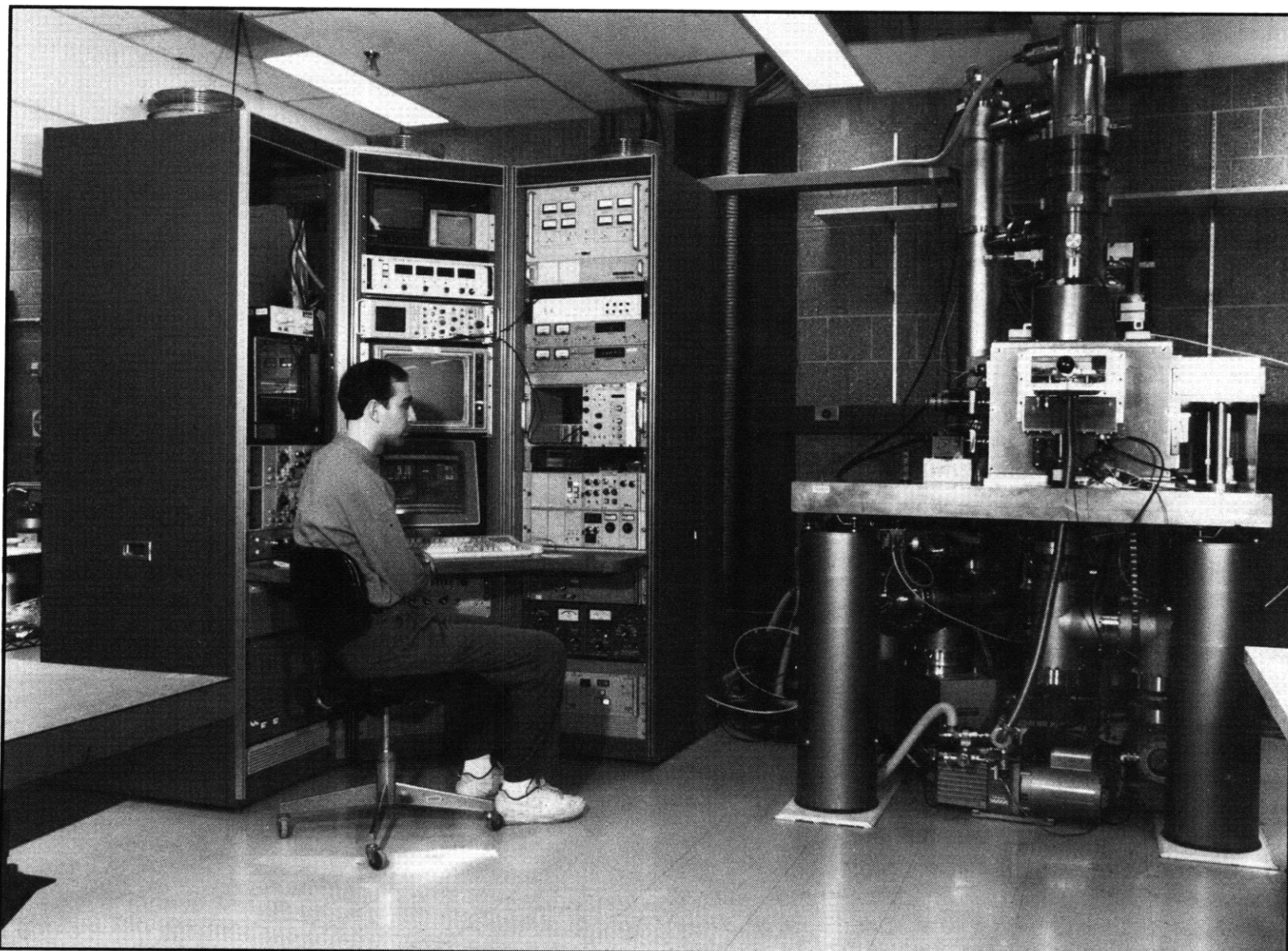

Figure 1. Photograph of the VS-PL scanning-electron-beam lithography system. The operator is Scott Silverman.

to pattern x-ray nanolithography masks for in-house use.

Figure 2 shows shows a region of an x-ray mask, patterned by the VS-PL tool with the gate level for deep-submicron silicon-on-insulator devices. This mask was then used in a mix-and-match scheme to fabricate the actual devices. Other projects include direct-write experiments on GaAs substrates oriented towards the fabrication of Coulomb-blockade devices; fabrication of photonic-bandgap resonator structures; and studies of MBE overgrowth of InP on patterned substrates for DFB lasers and optical filters.

5.3 Spatial-Phase-Locked Electron-Beam Lithography

Sponsors

Joint Services Electronics Program
Grant DAAH04-95-1-0038
National Science Foundation
Grant ECS 94-07078
Semiconductor Research Corporation
Contract 95-LJ-550
U.S. Army Research Office
Grant DAAH04-95-1-0564

Project Staff

James M. Carter, Juan Ferrera, Scott E. Silverman, Professor Henry I. Smith

It is well known that scanning-electron-beam lithography can write extremely fine lines, ~10 nm in thin PMMA and ~1 nm in AlF_3. However, because writing fields in electron-beam lithography are quite small (~10^4 beam steps), large-area patterns must be created by stitching together the small fields, using a laser interferometer to provide X-Y positioning information. However, it is often overlooked that, due to instability, drift and a variety of other problems, the precision with which this can be done is much poorer than the resolution. Typically, stitching errors of 30 to 100 nm are observed at field boundaries.

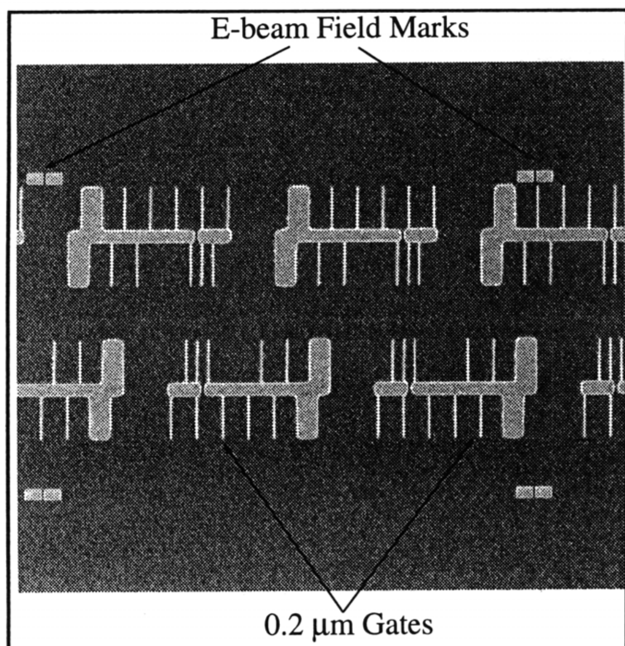

Figure 2. Scanning elecron micrograph of a portion of an x-ray mask patterned with the VS-PL e-beam system, showing the gate level for deep-submicron silicon-on-insulator devices.

To solve this problem, we are developing a technology we call spatial-phase-locked electron-beam lithography (SPLEBL), which will provide pattern placement accuracy and precision finer than the resolution. The basic idea behind SPLEBL is to create on the substrate a fiducial grid and conduct all e-beam lithography with reference to it. The fiducial grid is produced by interferometric lithography (IL) to ensure long-range spatial-phase coherence.

We are investigating two modes of implementation: the global fiducial grid and the segmented grid. In the latter approach, the grid is transferred onto the substrate only in small regions (2 x 2 μm square) at the corners of each e-beam scan field. Spatial-frequency-domain techniques are used to achieve sub-pixel alignment and scaling. In the latter approach the fiducial grid is transparent to the exposing e-beam and covers the entire top of the resist film. By collecting the emitted secondary electrons, a computer will keep track of the e-beam position at all times and correct for any drift or spurious displacement.

SPLEBL was used to pattern x-ray masks with gratings for the fabrication of integrated optical filters, in collaboration with IBM's T.J. Watson Research Center. Gratings with multiple quarter-wave phase shifts and duty cycle variations are needed to fabricate filters whose performance exceeds that of single quarter-wave-shifted resonators. For these applications, the flexibilty of e-beam patterning is essential, while spatial-phase locking eliminates the pattern placement errors, which would have a significant deleterious impact in the performance of the devices.

The suitability of fiducials produced by interferometric lithography for pattern placement with nanometer precision is being investigated. The grid must be characterized with precision equal or better that the pattern placement desired. We are developing techniques to measure the fidelity of gratings and grids fabricated by interferometric lithography. Figure 3 shows a schematic of the system used to fabricate fiducials. Two spherical waves, which emanate from the spatial filters, are overlapped at the substrate plane to produce a grating image in resist. This grating has a nonlinear phase progression, i.e., a "chirp". The phase deviation from linearity can be calculated from the geometrical parameters of the interferometric system. To confirm the validity of this model, we use a self-reference technique: a substrate is exposed in the IL system and displaced by a known distance; it is then exposed again. Thus, two identical grating images have been exposed, which are shifted with respect to each other. The nonlinearities in the phase progression of the gratings cause them to beat in and out of phase. Upon development, a moiré pattern appears on the surface of the sample, which is, in effect, a map of the difference in phase between the two gratings (see figure 4). The moiré qualitatively matches a theoretical phase map, indicating that no distortion larger than a fraction of the grating period (200 nm) is present. Work is under way to extend this technique to enable the quantitative measurement of phase distortions.

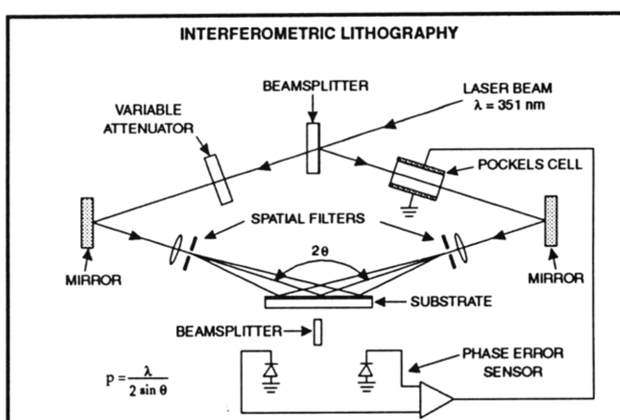

Figure 3. Schematic of the Interferometric Lithography (IL) system used to fabricate fiducial gratings and grids for spatial-phase locking. Mutually coherent spherical waves emanate from the spatial filters and are combined at the substrate to form a grating in resist. A grid is made of two gratings exposed at right angles to one another.

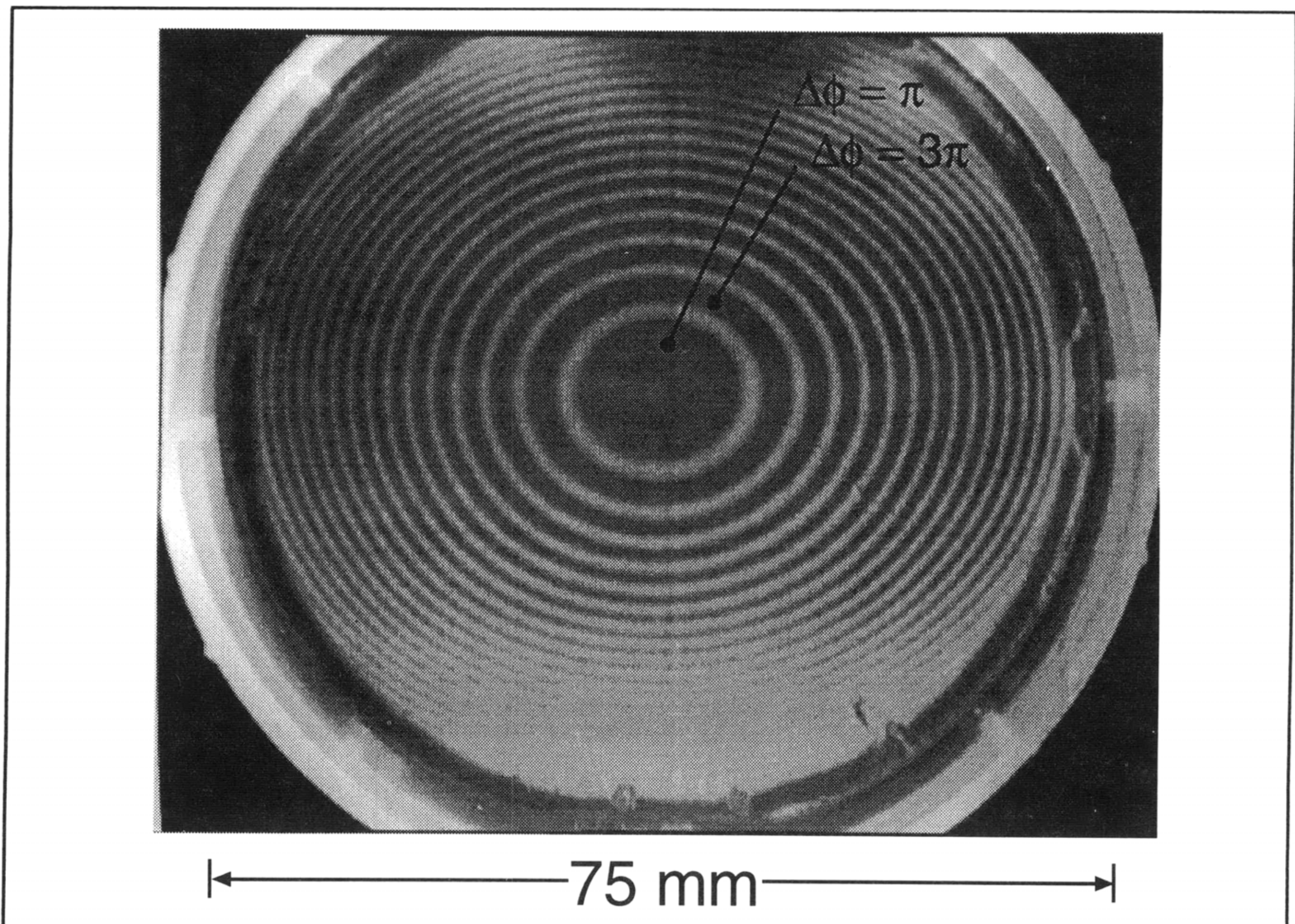

Figure 4. Photograph of a moiré pattern on a wafer, obtained by exposing two 200 nm-period gratings, with the substrate shifted laterally in between the two exposures. The moiré fringes denote the phase difference between the two exposures.

5.4 X-Ray Nanolithography

Sponsors

Defense Advanced Research Projects Agency/
Naval Air Systems Command
Contract N00019-95-K-0131
Joint Services Electronics Program
Grant DAAH04-95-1-0038

Project Staff

James M. Carter, Michael H. Lim, Euclid E. Moon, Vincent V. Wong, Isabel Yang, Professor Henry I. Smith

For several years, we have been developing the tools and methods of x-ray nanolithography (i.e., sub-100 nm features). We have explored the theoretical and practical limitations, and endeavored to make its various components (e.g., mask making, resists, electroplating, sources, alignment, etc.) reliable and "user friendly". Because of the critical importance of the x-ray mask technology we discuss this separately in section 5.5.

Our sources for x-ray nanolithography are simple, low-cost electron-bombardment targets, typically Cu_L (λ = 1.32 nm), separated by a 1.4 μm-thick SiN_x vacuum windows from a helium-filled exposure chambers. In the future, we hope to replace the Cu_L sources with higher flux sources.

For most applications that require multiple mask alignment, we currently use a simple microscope-based system which provides about 0.3 μm superposition precision. We are also developing a high-precision mask alignment system (see section 5.6) that should provide overlay approaching 1 nm.

In earlier research, we showed that for x-ray wavelengths longer than ~0.8 nm, the range of the photoelectron emitted when an x-ray photon is absorbed in resist does not limit the resolution. Down to feature sizes ~20 nm, diffraction is the major concern. By means of accurate electromagnetic calculations, taking into account the vectorial

character of the electromagnetic field and the dielectric properties of the absorber, we have shown that when source spatial coherence is optimized, diffraction does not limit resolution as severely as had been predicted by simple Fresnel diffraction calculations. Figure 5 plots the maximum mask-to-sample gap, G, versus minimum feature size, W, for two values of the parameter α which connects gap and feature size: $G = \alpha W^2/\lambda$. Modeling and experiment verify that α can be between 1 and 1.5 while retaining good process latitude.

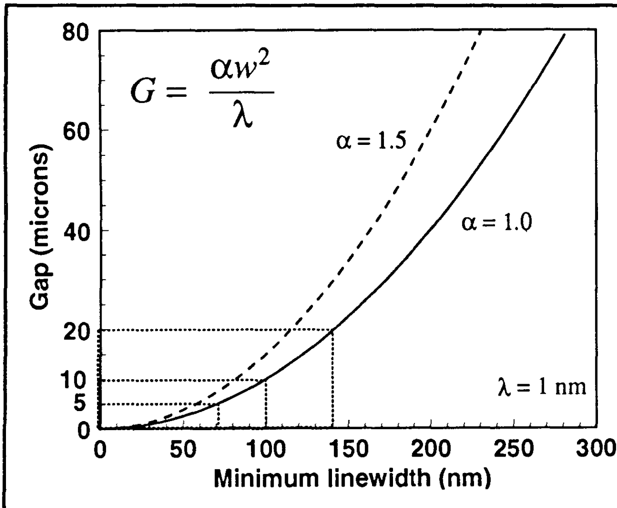

Figure 5. Plot of maximum mask-sample gap, G, versus minimum feature size, W, for two values of the parameter α.

For gaps below 10 μm, the mask and substrate must be optically flat (see section 5.5) and dust particles must be detected and eliminated. To accomplish this, a jet of frozen CO_2 micropellets impinging on the substrate or mask at a low angle can be used. The pellets knock off adhering dust particles while leaving no residue, and the CO_2 gas also tends to remove thin layers of organic contamination.

For the linewidth range from 70 to 20 nm, mask-substrate gaps must be below 5 μm. This is not a problem in a research setting. With wafer type substrates, we use small studs on the perimeter of the mask to achieve the required gap. On substrates that are smaller than the mask area (e.g., fragments of high-mobility, modulation-doped GaAs substrates), we use a specially designed apparatus that brings the mask membrane to zero gap without damaging either mask or substrate. In manufacturing, however, studs on the mask and mask contact are not acceptable, and for this reason we are investigating the feasibility of using arrays of Freznel zone plates for projection imaging with x rays of either 4.5 nm or about 1.0 nm wavelength.

5.5 Improved Mask Technology for X-Ray Lithography

Sponsors

Defense Advanced Research Projects Agency/
U.S. Navy - Naval Air Systems Command
Contract N00019-95-K-0131
Joint Services Electronics Program
Grant DAAH04-95-1-0038

Project Staff

Martin Burkhardt, James M. Carter, Andrea E. Franke, Michael H. Lim, Mark K. Mondol, Edward Murphy, Vincent V. Wong, Isabel Y. Yang, Professor Henry I. Smith

At feature sizes of 100 nm and below, the mask-to-sample gap, G, must be less than ~10 μm (see figure 5). We have developed a mask configuration compatible with this requirement in which the mask membrane is flat to ~100 nm, as shown in figure 6. A novel, low-gradient furnace was developed to achieve such high levels of mask flatness.

Our mask technology is based on low-stress, Si-rich silicon nitride, SiN_x. This material is produced in the Integrated Circuit Laboratory at MIT in a vertical LPCVD reactor. The resulting films are clean and uniform, and x-ray mask membranes made from them are extremely robust. They can be cleaned and processed in conventional stations. Radiation hardness remains a problem at dose levels corresponding to production (i.e., millions of exposures). For research purposes, however, the material is fully acceptable.

For absorber patterns we use both gold, Au, and tungsten, W. The gold is electroplated onto the membrane after resist exposure and development using a specially designed apparatus. The stress of the gold, which affects the in-plane distortion, is controlled via the plating conditions. We generally try to achieve a stress below 10^7 Mpa. The W is sputter deposited and patterned by reactive-ion etching. In order to ensure uniform W stress over an entire membrane, a He-backside temperature-homogenization apparatus is used. This produces stress that is uniform to within about 5 Mpa over most of the membrane, but higher near the edges. The edge deviation is attributed to inadequate heat flow control. We are currently investigating schemes to fully homogenize the stress over the entire membrane.

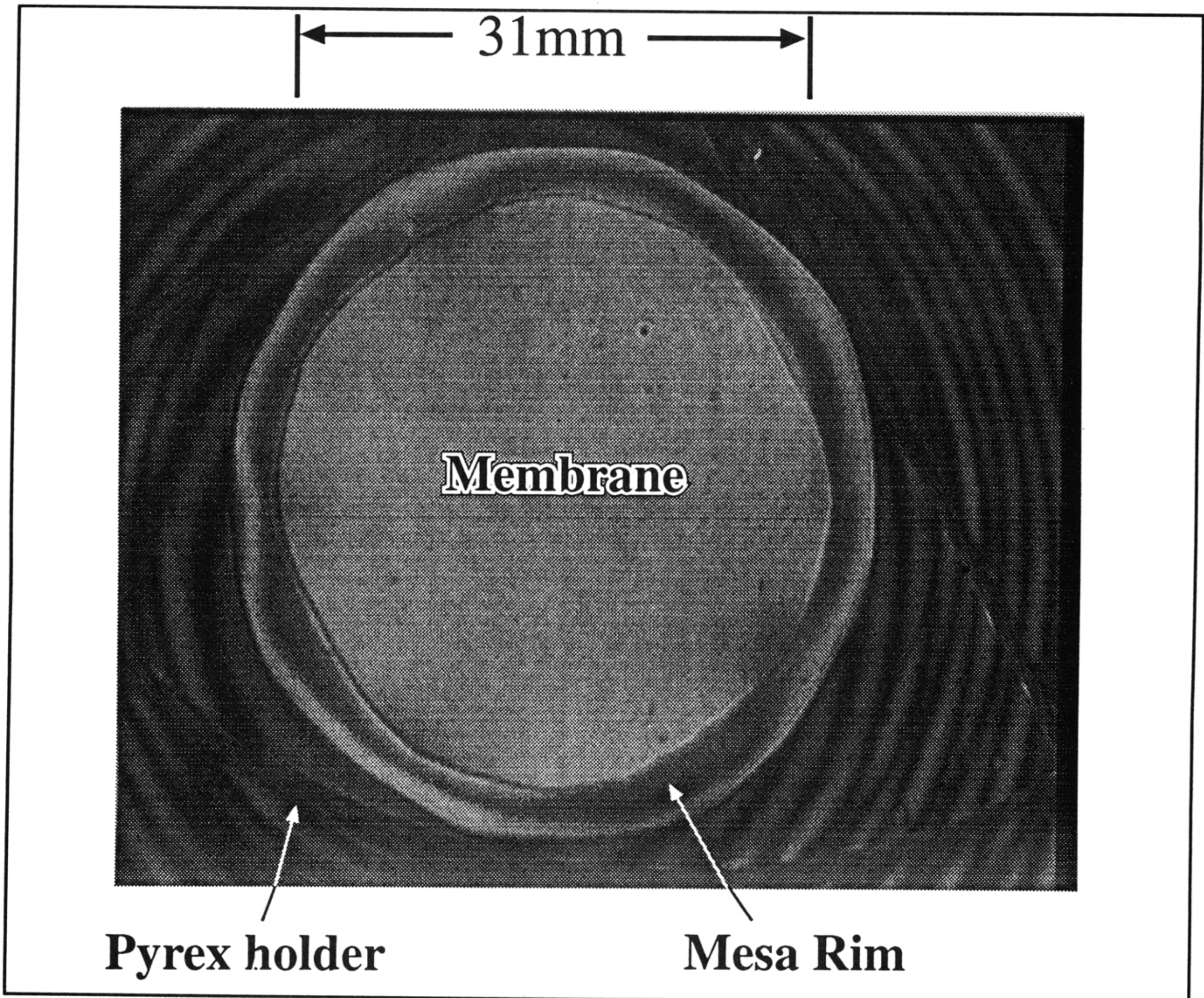

Figure 6. Fizeau interferogram of the top surface of an x-ray mask fabricated with the low gradient oven. There are no fringes visible over the membrane area indicating a flatness ~100 nm. The mesa rim deviates from perfect flatness by ~300 nm. The area outside the mesa rim is a pyrex frame, whose deviation from flatness is of no significance.

We are investigating a scheme for edge reinforcement, illustrated in figure 7. The overhang of B-doped Si, several micrometers thick, provides a transition between the rigid Si mesa rim, and the thin membrane. Along the edge of the Si mesa rim there are often sharp asperities due to the etching process. These sharp, rigid points increase the probability of accidental membrane breakage. The overhang should prevent this, making the masks more suitable for a production environment.

For periodic structures, patterning of x-ray masks is done by interferometric lithography (IL) but for patterns of arbitrary geometry, it is done by e-beam lithography, either in the MIT e-beam facility or in collaboration with NRL or IBM. We use CAD tools at MIT and convert the data into formats compatible with the e-beam exposure systems. Data is shipped to NRL or IBM over the internet. After e-beam exposure, masks are shipped back to MIT by express mail where development and Au electroplating are carried out. This collaboration has already demonstrated that patterning x-ray masks by e-beam can be done remotely.

The recently acquired Digital Instruments STM/AFM was found it to be highly effective in inspecting x-ray masks, providing information on defects not apparent by other means. This is illustrated in figure 8.

For etching W absorber patterns on x-ray masks, a reactive-ion-etching process is required, which puts considerable power into the membrane substrate. Since membranes have very low thermal mass and conductivity, we use He-backside cooling in a reac-

tive ion etcher. Membranes can be cooled to below -20 C. At such low temperatures the isotropic etching component is suppressed leading to highly directional etching.

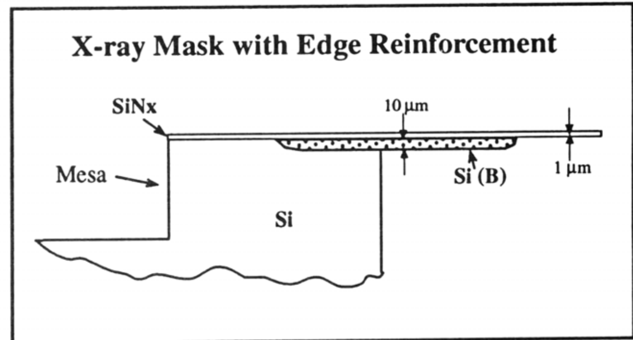

Figure 7. Schematic cross section of the edge reinforcement scheme being investigated to improve the robustness of x-ray masks. The overhang of B-doped Si, several micrometers thick, provides a transition between the rigid mesa rim and the 1-μm-thick membrane.

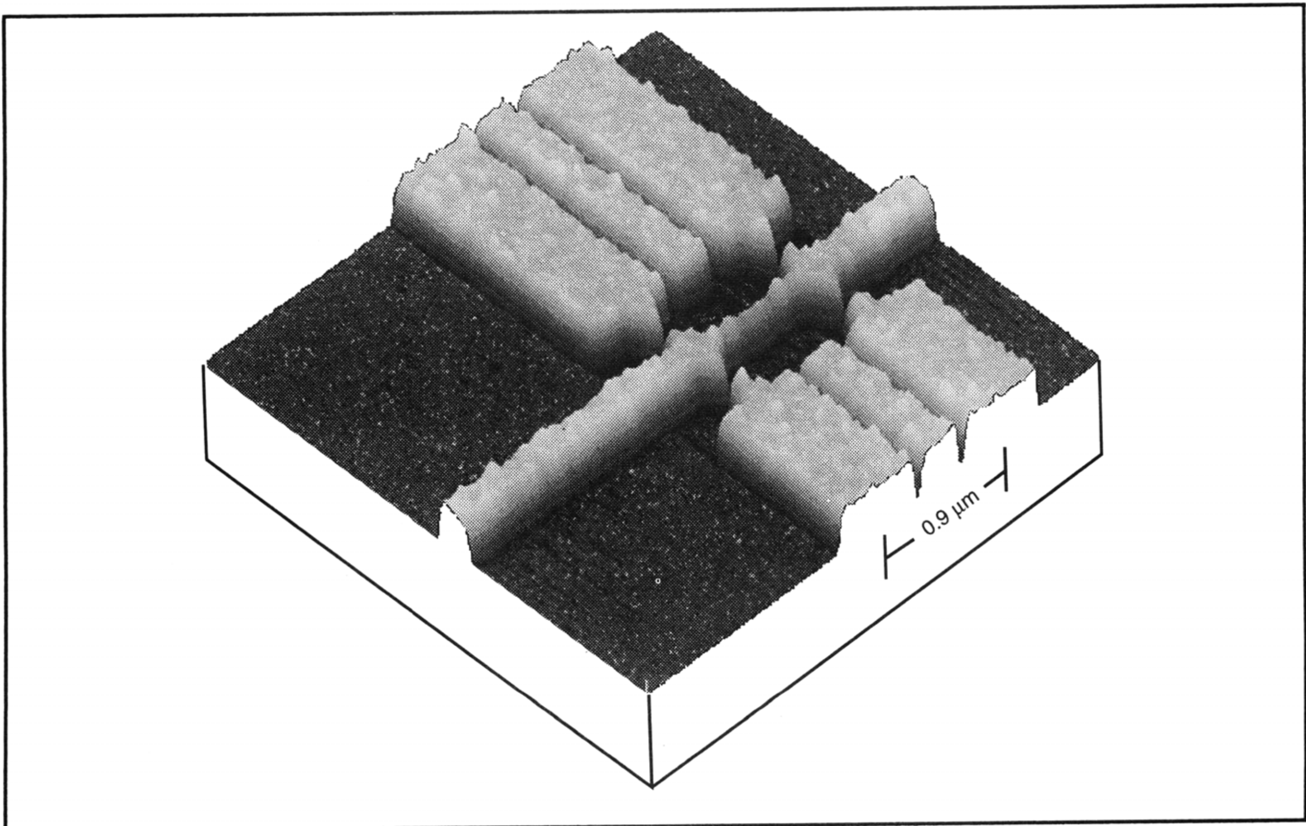

Figure 8. Inspection of an x-ray mask using the newly acquired Digital Instruments atomic-force microscope (AFM). This micrograph revealed that the plated gold in this pattern of a quantum-effect device was only 100 nm instead of the required 200 nm. This thickness deficiency was not apparent by SEM analysis.

5.6 A High-Precision Mask Alignment and Gapping System with Immunity to Overlayers

Sponsors

Defense Advanced Research Projects Agency/
Naval Air Systems Command
Contract N00019-95-K-0131
Joint Services Electronics Program
Grant DAAH04-95-1-0038

Project Staff

Patrick N. Everett, Euclid E. Moon, Professor Henry I. Smith

A novel x-ray lithographic alignment scheme termed interferometric broad-band imaging (IBBI) has been implemented and tested with a variety of wafer overlayers, such as resist, aluminum, and polysilicon. IBBI alignment employs grating and grid type alignment marks on mask and substrate, respectively, which are viewed through the mask from outside the x-ray beam at a Littrow angle with f/10 optics and a 110 mm working distance. Each mark consists of two gratings. When aligned, a grating period p_1 on mask is exactly above a grating period p_2 on wafer, with adjacent pair of gratings vice-versa. Gratings on wafer are "hatched" to enable Littrow diffraction in a plane parallel to the grating lines. This allows the optics to be offset in that plane to not obstruct the x-rays. Diffraction perpendicular to the grating-lines results in moiré fringes in the image plane. Using a CCD camera, misalignment is measured from two identical sets of moiré fringes (~50 mm period) that move in opposite directions as the mask is moved relative to the substrate. Alignment corresponds to matching the spatial phases of the two sets of fringes.

To demonstrate the insensitivity to overlayers, an alignment mark was partially covered with an overlayer. The resulting moiré pattern is shown in figure 9. Alignment was measured in each half of the image (i.e., with and without the overlayer) and the difference plotted in figure 10. With each of these overlayers, the mean alignment error between the regions is shown to be 0.2 nm or less.

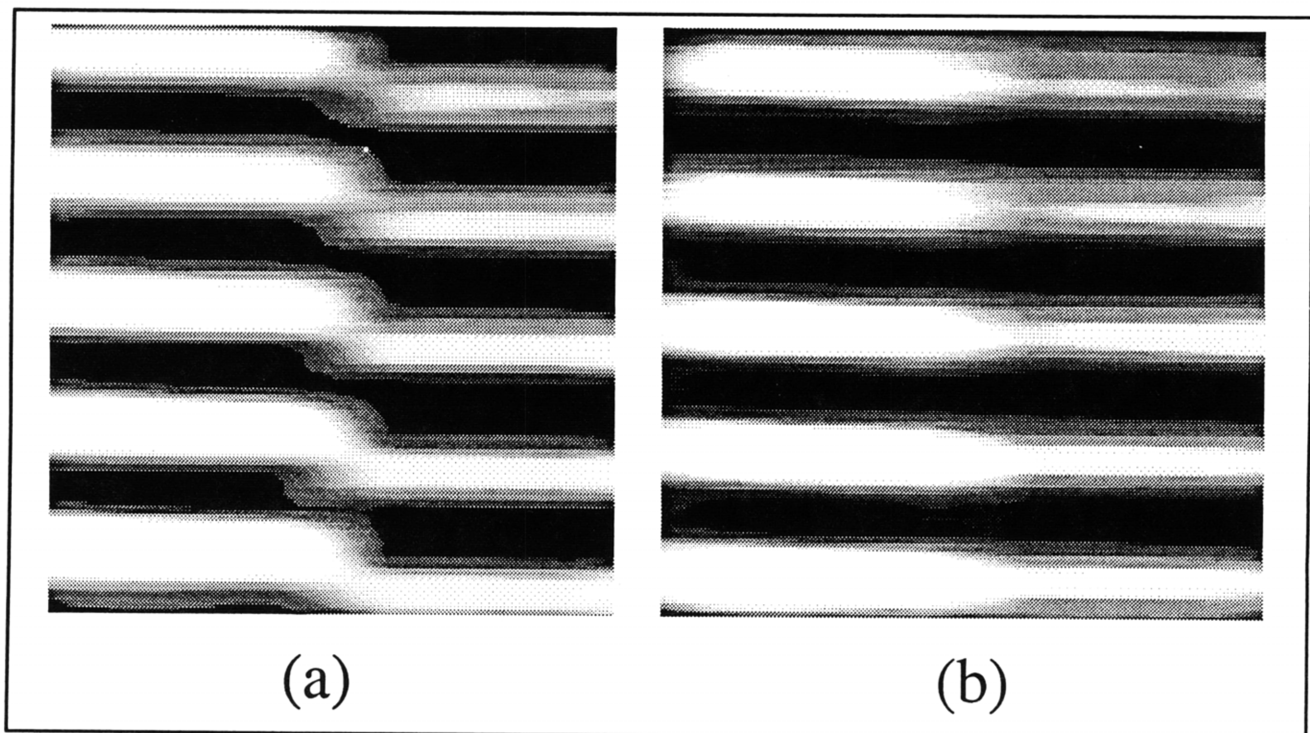

Figure 9. Interference fringes (moiré pattern) as seen by CCD camera in (a) misaligned and (b) aligned positions.

Gap is an important parameter in x-ray lithography, both to avoid mask-wafer contact and to ensure control of feature linewidth. To detect gap to high precision we have developed an interferometric gap detection scheme. This scheme uses the same marks and optics as employed in alignment, but viewed from a direction perpendicular to the grating lines. When viewed (and illuminated) in this orientation, the mask mark acts as a quasi-Michelson interferometer, with the grating being the beamsplitter, and the arms being the thickness of the mask membrane and the gap between the mask and wafer. No corresponding mark is required on the wafer. Illuminating the mask mark

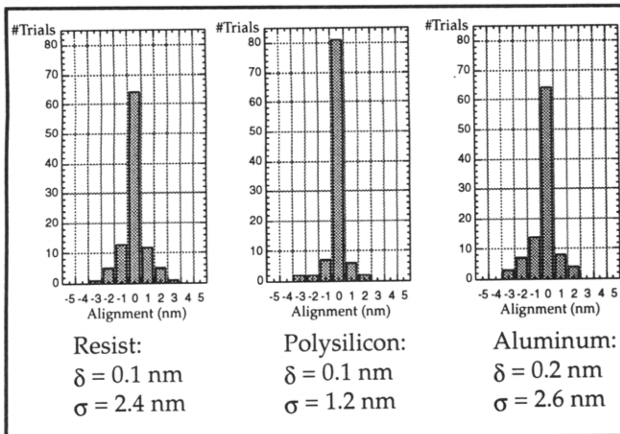

Figure 10. Effect of overlayers on alignment. For each overlayer, a histogram of 100 measurements is shown of the difference in spatial phase discontinuity between the half of the alignment mark with the overlayer and the half without the overlayer.

with polychromatic light results in an intensity variation as a function of gap. During a limited scan of gap, a beat pattern is obtained on each of the two sides of the mark. Since the beat periods are determined by the periods of the gratings, comparing these beat patterns yields an unambiguous measure of gap. The gap sensitivity of this method is better than 100 nm, which is sufficient for sub-100 nm lithography.

An x-ray source is being constructed to complete the prototype IBBI stepper/exposure system (figure 11). The nanometer-level alignment precision of this system will be essential in the fabrication of novel devices such SOI-MOSFET devices with gates both above and below the Si channel.

5.7 Interferometric Lithography

Sponsors

Joint Services Electronics Program
Grant DAAH04-95-1-0038
National Aeronautics and Space Administration
Contract NAS8-38249
Grant NAGW-2003

Project Staff

James M. Carter, Juan Ferrera, Robert C. Fleming, Timothy A. Savas, Dr. Mark L. Schattenburg, Satyen Shah, Professor Henry I. Smith

Interferometric (also called holographic) lithography schemes are preferred for the fabrication of periodic

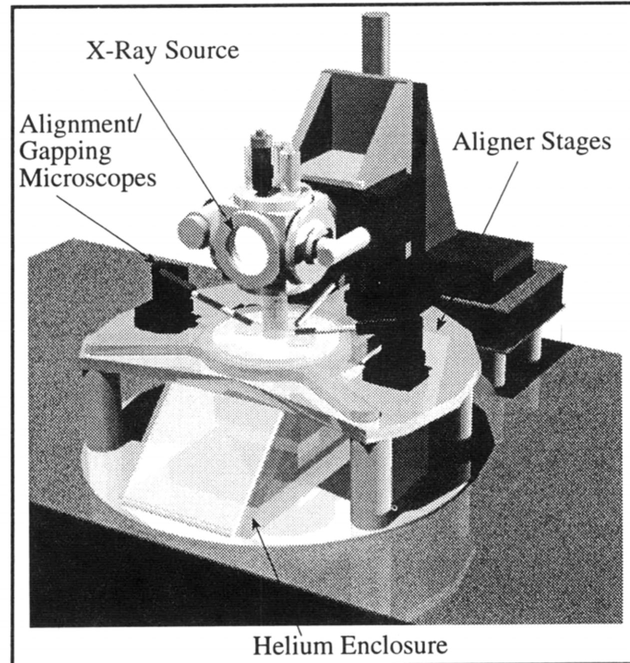

Figure 11. Interferometric broad-band imaging mask alignment/exposure system.

and quasi-periodic patterns that must be spatially coherent over large areas, and free of phase errors. For spatial periods down to 200 nm, an argon ion laser is used in a Mach-Zehnder configuration with a unique fringe-locking feedback system. This produces large area (10 cm diameter) gratings with long-range spatial-phase coherence, free of phase errors or detectable distortion. The fringe locking ensures reproducibility of exposure. A multiple exposure moire techniques is used to verify freedom from distortion (see section 5.3).

For spatial periods below 200 nm, bright light sources with wavelengths below 200 nm must be used. Such sources have limited temporal coherence, and thus one is forced to employ an achromatic scheme such as shown in figure 12. The source is an ArF laser (193 nm wavelength). A collimating lens, polarizer, and a scanning system are interposed between the source and the interferometer in order to achieve reasonable depth-of-focus and large exposure areas. We also use a white light interference principle to ensure equal path lengths in the two interferometer arms. Using this system, gratings and grids of 100 nm period (nominally 50 nm lines or posts) are obtained in PMMA on top of a specially designed antireflection coating. Figure 13 shows a 100 nm period grid etched into Si following achromatic interferometric lithography.

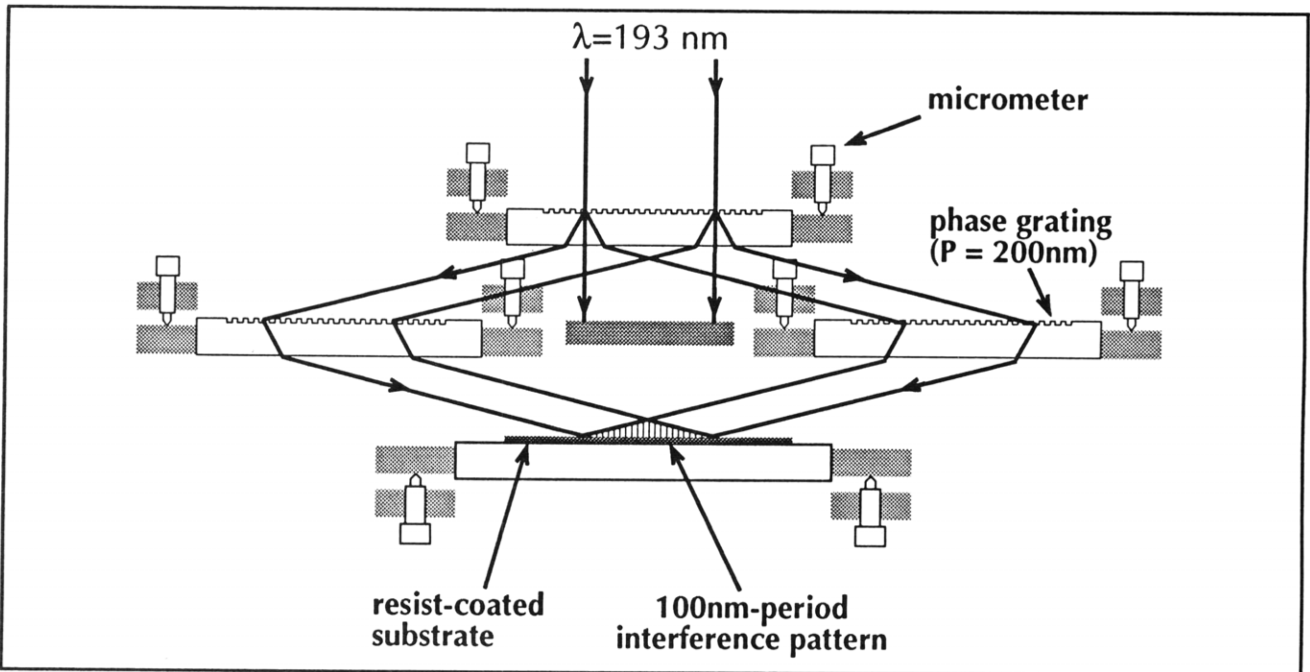

Figure 12. Achromatic interferometric lithography (AIL) configuration.

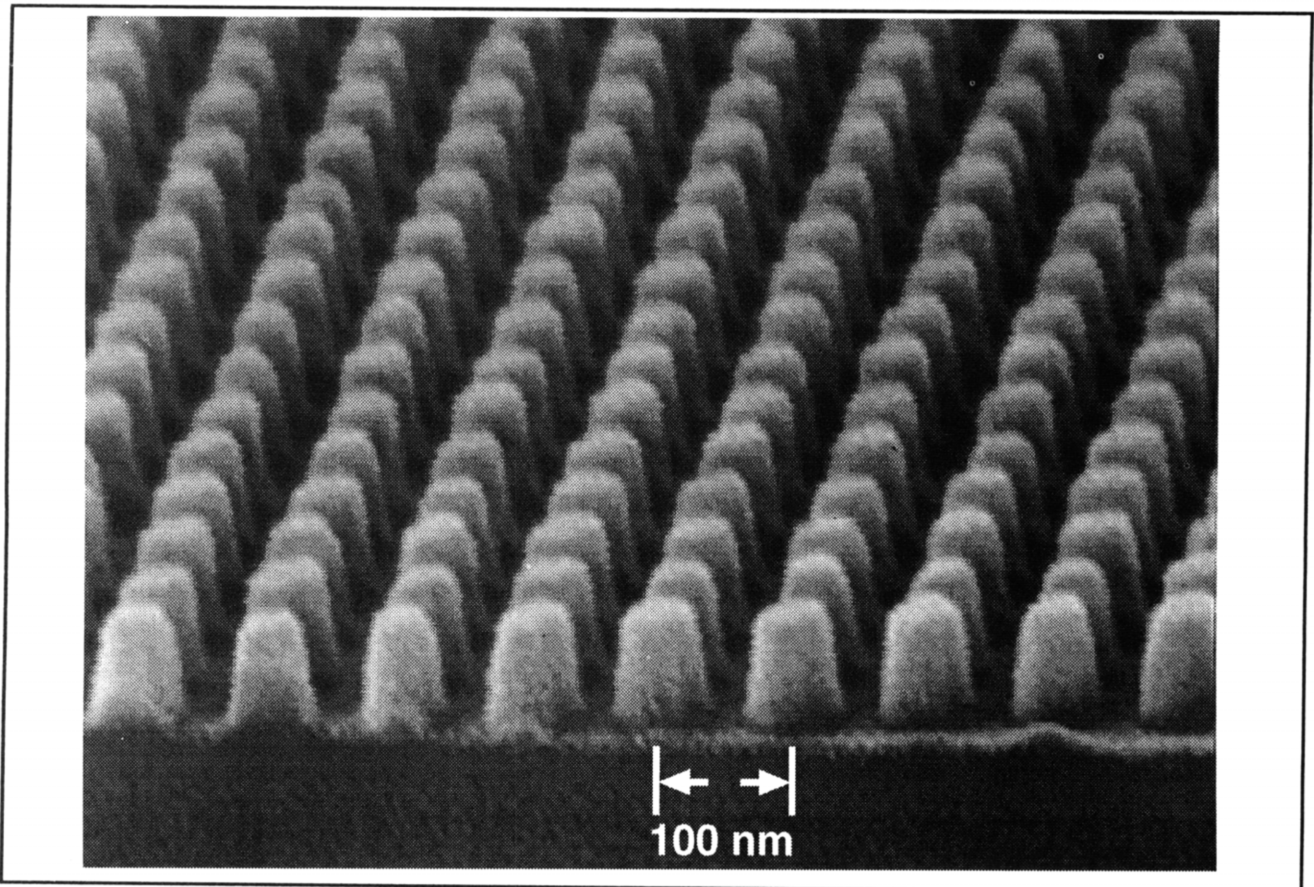

Figure 13. Scanning electron micrograph of a 100 nm period grid, exposed in PMMA on top of a specially designed antireflection coating, and transferred into Si by reactive ion etching.

Grids such as shown in figure 13 are of interest in a number of applications including high-density magnetic information storage and flat-panel displays based on field emission. At present, we use interferometric lithography to produce grid exposures of 200 and 320 nm period for a flat-panel-display program at MIT Lincoln Laboratory. In the future, we expect to provide similar grids for Professor Akinwande who also conducts research on flat-panel displays.

5.8 Ion-Beam Lithography

Sponsor

Joint Services Electronics Program
Grant DAAH04-95-1-0038

Project Staff

Scott E. Silverman, Professor Henry I. Smith, Professor Carl V. Thompson, Anto Yasaka

Yields of FIB-induced secondary electron from Si, Al, and PMMA targets have been measured to investigate the feasibility of spatial-phase-locked FIB lithography. The results indicate that Al has very high secondary electron yield ranging from 5.7 to 6.9 electrons per ion for 120-240 keV Si^{2+} incidence, and PMMA has very low secondary yield, ranging from 1.0 to 1.5 electrons per ion for the same ion irradiation conditions. These results lead to the conclusion that a fiducial grid fabricated on a substrate will be imaged with sufficient contrast by detecting FIB-induced secondary electrons. Furthermore, the image obtained by FIB will have a much better signal-to-noise ratio than the image obtained by electron beams because of the fact that ion bombardment produces almost no backscattering electrons. The required ion dose to detect the fiducial-grid signal with appropriate contrast was calculated. This value is much lower than the ion dose required to expose resist. Thus, it is possible to detect the grid signal without disturbing the writing. It seems reasonable to conclude that spatial-phase-locked FIB lithography will be a promising tool to produce nanometer range resolution lithography with high accuracy and precision.

Secondary electron yields as a function of ion irradiation time were also measured. When plotting the results of the secondary yields versus time, considerable differences in the tendency of the curves are observed depending on the target materials. An explanation of the observed results was attempted in terms of two competing processes: sputtering by incident ions and oxidation by residual gases. For a Si target, the results can be illustrated quite naturally as due to the two processes. That is, removal of native oxide by sputtering results in a decrease of secondary yield with time for high current density, and for low current density the surface remains oxidized due to reaction of residual gases and the surface atoms and thus the secondary yield shows little change with time. For an Al target, however, this model cannot explain all of the observed results. In some cases, an increase of the secondary yields with time has been observed.

5.9 High Performance Self-aligned Sub-100 nm MOSFETs using X-ray Lithography

Sponsors

Defense Advanced Research Projects Agency/
Naval Air Systems Command
Contract N00019-95-K-0131
IBM Corporation
Contract 1622
Joint Services Electronics Program
Grant DAAH04-95-1-0038
U.S. Navy- Office of Naval Research
Grant N00014-95-1-1297

Project Staff

James M. Carter, Keith M. Jackson, Isabel Y. Yang, Professor Dimitri A. Antoniadis, Professor Henry I. Smith

We have fabricated sub-0.1 μm N-channel MOSFET devices on bulk Si using x-ray lithography. Extremely well controlled short-channel effects were achieved through appropriate channel and source/drain engineering. Figure 14 shows the device schematic. The retrograde channel doping profile was accomplished using shallow indium and deep boron implants. The source/drain halo extensions were formed using a low energy arsenic implant with indium preamorphization and counterdoping. The self-aligned polysilicon gates were fabricated using x-ray nanolithography and an anisotropic etching process. The aligned microgap x-ray exposures were carried out using mesa-etched SiN_x x-ray masks with Au absorber pattern. Hot Carrier Degradation of the 0.1 μm N-channel MOSFETs devices has been examined with results suggesting that a Vdd of around 1.6 V gives a lifetime of 10 years for 0.1 μm devices fabricated in this lot.

Current work on sub-0.1 μm devices on bulk Silicon is focusing on N-channel MOSFETs designed to work at 77 K where further improvement of device characteristics occurs. Measurements show that the devices turn on and off more sharply (the sub-

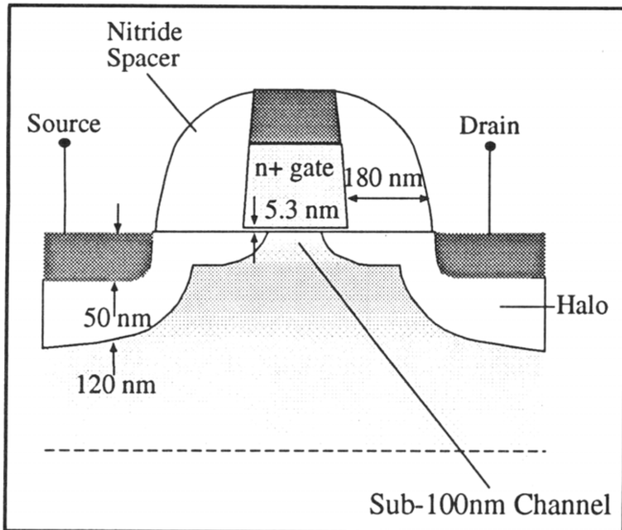

Figure 14. Schematic of 0.1 μm channel-length self-aligned NMOSFET.

threshold slope improves from 80 to 24 mV/decade) and the transconductances are at least 50 percent higher at 77 K, see figure 15. Future work will address fabrication of devices optimized for low temperature operation, performance improvements, and hot carrier reliability.

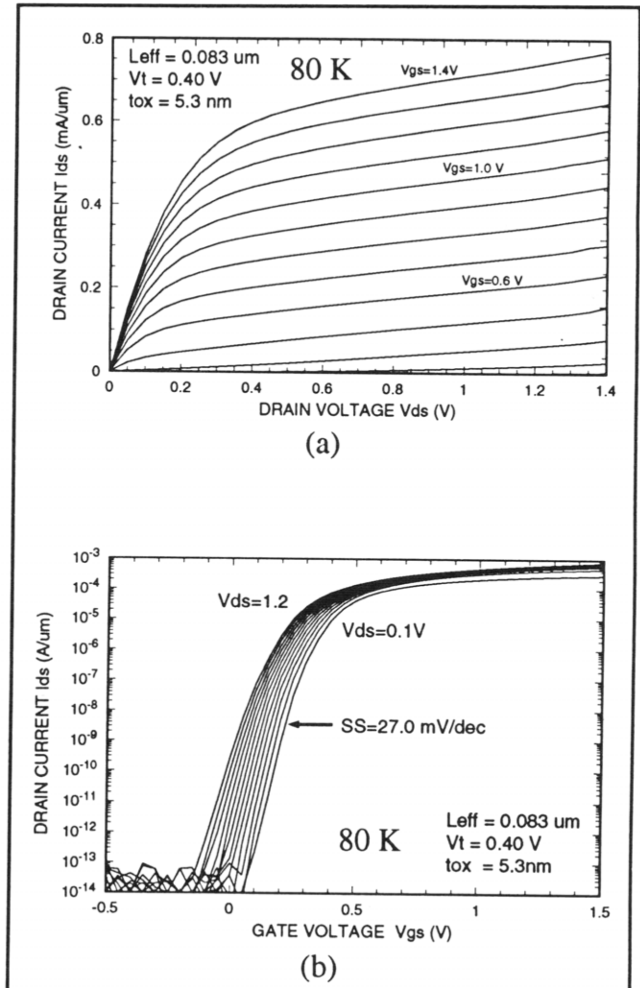

Figure 15. I-V characteristics of an 83 nm-channel-length NMOSFET cooled to 80 K.

5.10 Single and Dual-Gate SOI Devices

Sponsors

Defense Advanced Research Projects Agency/
Naval Air Systems Command
Contract N00019-95-K-0131
IBM Corporation
Contract 1622
Joint Services Electronics Program
Grant DAAH04-95-1-0038
U.S. Navy- Office of Naval Research
Grant N00014-95-1-1297

Project Staff

James M. Carter, Keith M. Jackson, Isabel Y. Yang, Professor Dimitri A. Antoniadis, Professor Henry I. Smith

Our current work aims to extend the 100 nm device technology to a full CMOS line, on bulk as well as on SOI substrates. Two different device structures are explored on the SOI substrates. One is the conventional structure on SOI, and the other is the double-gated structure (SOIAS) with a top gate having deep-submicron length, and a wider bottom gate.

Our first effort is to get a fundamental understanding of these devices in DC; i.e., short channel effects, drain-induced barrier lowering (DIBL), coupling of the backgate to the front gate, etc. Currently, the backgate is defined by ion implantation through the top using optically exposed thick resist as the mask. The top gate is then aligned over this bottom gate via x-ray lithography. The technology issue here is the mixing and matching of the optical stepper to the e-beam tool which writes the patterns on the x-ray masks.

We have developed a technique to do this matching that also saves e-beam writing time. Figure 16 shows this process in which the coarse patterns, e.g., pads and e-beam field alignment marks, are first transferred onto a chrome coated quartz wafer using the optical stepper. The pattern is then transferred into chrome by a wet etch. A one-to-one pattern transfer of the coarse features onto the x-ray mask is then done using proximity 240 nm UV exposure. The coarse patterns and the field alignment marks are then plated up in Au and sent to the e-beam for fine pattern writing. The final pat-

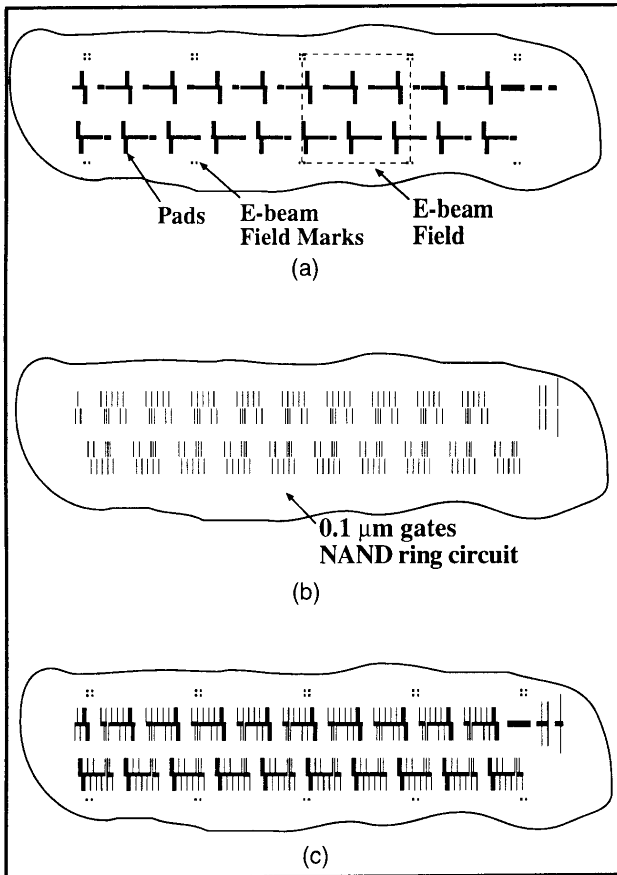

Figure 16. Sketch of a small portion of the chip showing: (a) a pattern of coarse features (pads) transferred onto the x-ray mask by deep UV lithography; (b) fine features written by e-beam lithography; (c) composite of fine and coarse features on the x-ray mask. The pattern is a nand ring circuit.

terns on the mask will have coarse features patterned by UV proximity printing and fine features written by e-beam lithography, as depicted in figure 16c.

We were able to fabricate CMOS devices on bulk, SOI and SOIAS substrates with this mix-and-match scheme with device lengths of 0.2 μm. Figure 17 shows the subthreshold characteristics of a backgated device made on SOIAS substrate. The backgate can control the NMOS and PMOS threshold voltages independently from the front-gate and from each other. Thus, making dynamic control of threshold voltage for low power applications possible.

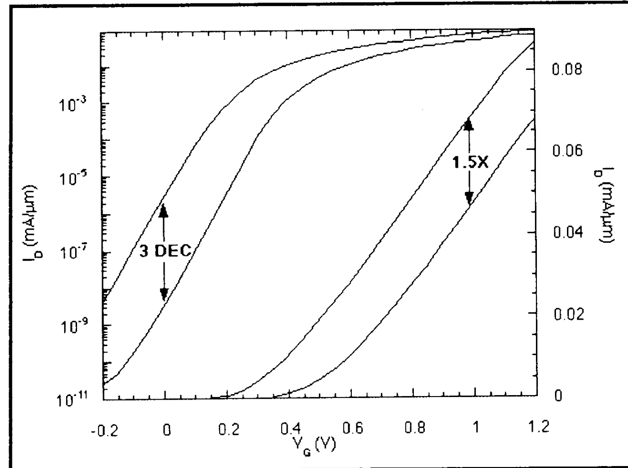

Figure 17. Subthreshold characteristics of an Leff=0.2 μm device on linear and log scale showing 3 decade reduction in off current and 1.5 times increase in drive current when the threshold voltage is switched.

5.11 Fabrication of T-gate Devices using X-ray Lithography

Sponsor

U.S. Army Research Office
Grant DAAH04-94-G-0377

Project Staff

Mitchell W. Meinhold, Professor Henry I. Smith

Monolithic microwave integrated circuits (MMICs) have potential applications in automobile navigation, collision-avoidance, and wireless communication systems. The high-speed MODFET devices of such circuits require very short gate lengths, while preserving low resistance. Large gate widths are required for high current drive. To meet these conflicting demands so-called "T-gate" and "gamma-gate" processes are used in which the base or stem of the gate is very short (~100 nm) while the upper part is large, overlapping the stem, similar to a mushroom, or the letters T or Γ. Although such structures can be achieved using direct-write electron-beam lithography in double-layer resists, the technology is expensive, slow, and unlikely to meet future production needs. For these reasons, we are developing a process for fabricating T-gates using x-ray lithography.

The fabrication sequence is shown in figure 18. The first layer defines the stem of the gate, a critical parameter for a field-effect device. After exposing and developing the first layer, a second layer of resist is deposited and the pattern corresponding to the upper part of the gate exposed.

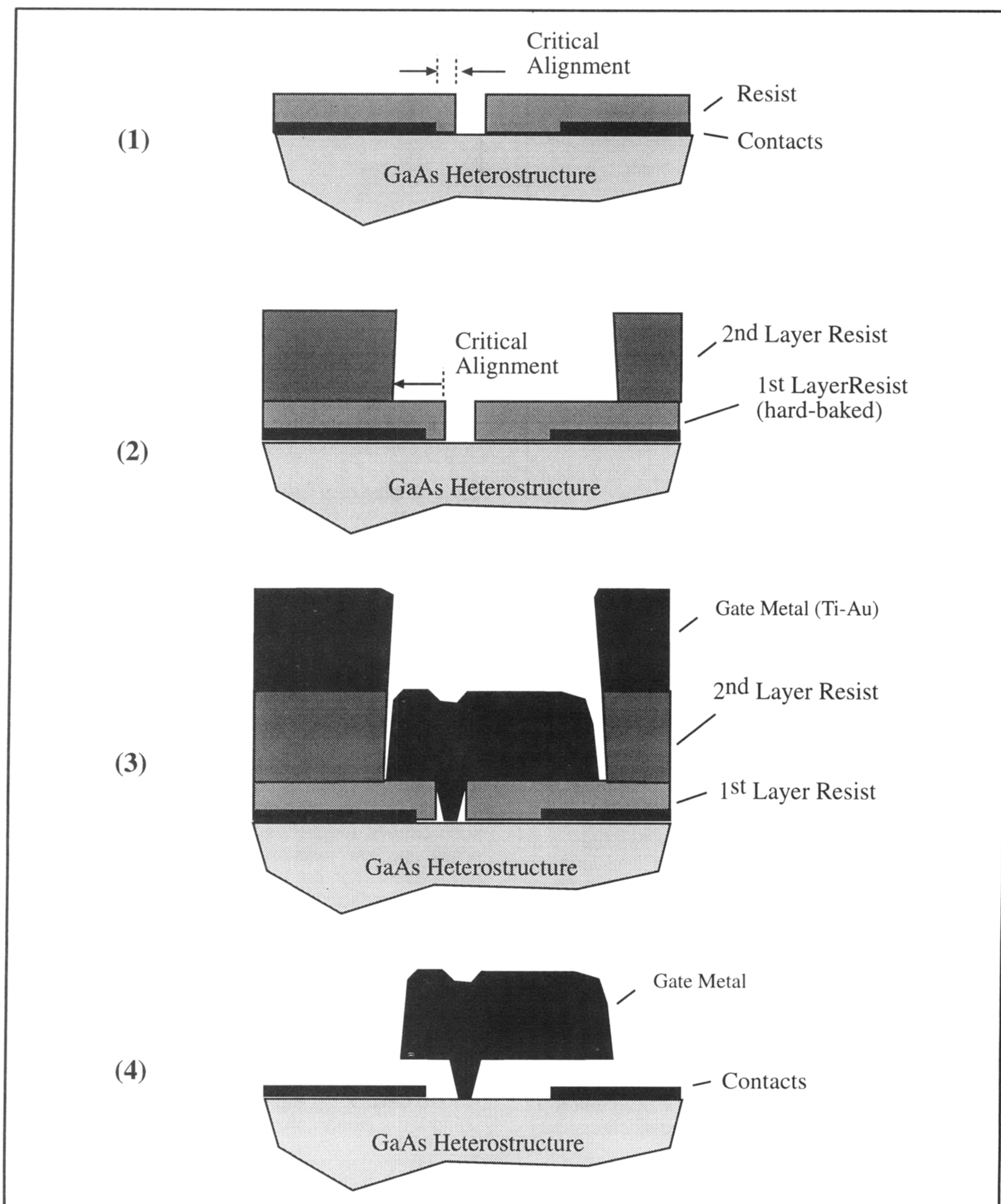

Figure 18. Depiction of the T-gate process steps: (1) Resist is deposited over existing contact metal. Alignment and exposure takes place. (2) After hardening the first layer, a second layer is deposited. The second pattern alignment and exposure takes place. (3) Gate metal is deposited. (4) Liftoff (resist removal)

At this point, gate metal can be deposited forming the T-gate. There are two challenges to achieving this process. First, it must be possible to align the x-ray masks to within 100 nm. Second, if the masks do not share a common coordinate system, features such as the gate stem and mushroom will not align properly. Also, without precision mask alignment it would not be possible to get the gate stem very close to the source. Therefore, the three x-ray masks required in the process depicted in figure 18 must be written with reference to a coordinate system that is common to all the masks. To meet the first challenge, we have put alignment marks on the masks that are compatible with the high precision, IBBI alignment system (see Section 5.6). We anticipate no difficulty in achieving sub-100 nm alignment with the IBBI system.

To meet the second challenge, x-ray masks are prepared with a grid array of reference marks located at the corners of fields measuring 0.1 x 0.1 mm, the field size of the e-beam lithography system. These reference marks were transferred to each x-ray mask with DUV lithography using the same optical mask, thereby guaranteeing a common coordinate system for all three x-ray masks. Upon registration to these marks, the e-beam lithography system should be able to place patterns with a precision well below 100 nm.

There are a number of interesting directions that may be followed once a reliable, high latitude process is established. For manufacturable MMIC systems, both MESFETs and HEMTs are required for low-noise and power applications. Initially, relatively simple GaAs MESFETs will be studied, followed by GaAs and InP HEMTs of varying degrees of complexity. Further studies could include low-temperature-grown GaAs MESFETs for high breakdown voltages, self-aligned devices, or gate materials other than Au such as W.

5.12 Studies of Coulomb Charging Effects and Tunneling in Semiconductor Nanostructures

Sponsors

Joint Services Electronics Program
Grant DAAH04-95-1-0038
U.S. Air Force - Office of Scientific Research
Grant F-49-620-92-J-0064

Project Staff

Martin Burkhardt, David J. Carter, Ilia Sokolinski, Professor Dimitri A. Antoniadis, Michael R. Melloch,[1] Professor Terry P. Orlando, Professor Henry I. Smith

Quantum-effect devices, whose minimum feature sizes are comparable to the Fermi wavelength (about 50 nm in a typical inversion layer), have promising potential in novel electronics applications. Quantum-dot devices have drawn particular attention. In such devices an electron gas is confined electrostatically in all three dimensions, forming a small "island" of electrons ~100 nm, bounded on all sides by potential walls. This small electron "island" resembles an atom because there can be only an integer number of electrons, and these electrons can occupy only certain discrete energy levels. If two dots are coupled, a structure resembling a molecule is obtained. The conductance of the dot, when connected to leads through tunneling barriers, exhibits strong oscillations as the voltage of the gate is varied. Each successive conductance maximum corresponds to the addition of a single electron to the dot. At temperatures in the mK range, the conductance decreases by orders of magnitude in between adjacent conductance maxima because there is a large energy cost for an electron in the lead to enter the dot. This energy cost can be removed by changing the gate voltage, resulting in the observed periodic dependence of the conductance on gate voltage. This depends on how fast the chemical potential within the dots is changed for a change in gate voltage. For two arbitrary dot sizes and very low temperature, the conditions for conductance through the dots are arbitrary, and conductance events are expected to be stochastic.

Figure 19 is a schematic of a coupled-quantum-dot device. The dots are formed in a two-dimensional electron gas (2DEG) in an MBE-grown GaAs/AlGaAs heterostructure. The 2DEG is approximately 60 nm below the surface of the material. The 2DEG is contacted electrically with ohmic contacts, depicted in the corners, and the 2DEG is confined laterally with Schottky gates which repel the electrons underneath. The areas where the 2DEG exisits are shown in light grey. The two quantum dots (the isolated "islands") are connected to the 2DEG leads by quantum point contacts (QPCs) and to each other by a thin tunnel barrier.

[1] Purdue University, West Lafayette, Indiana.

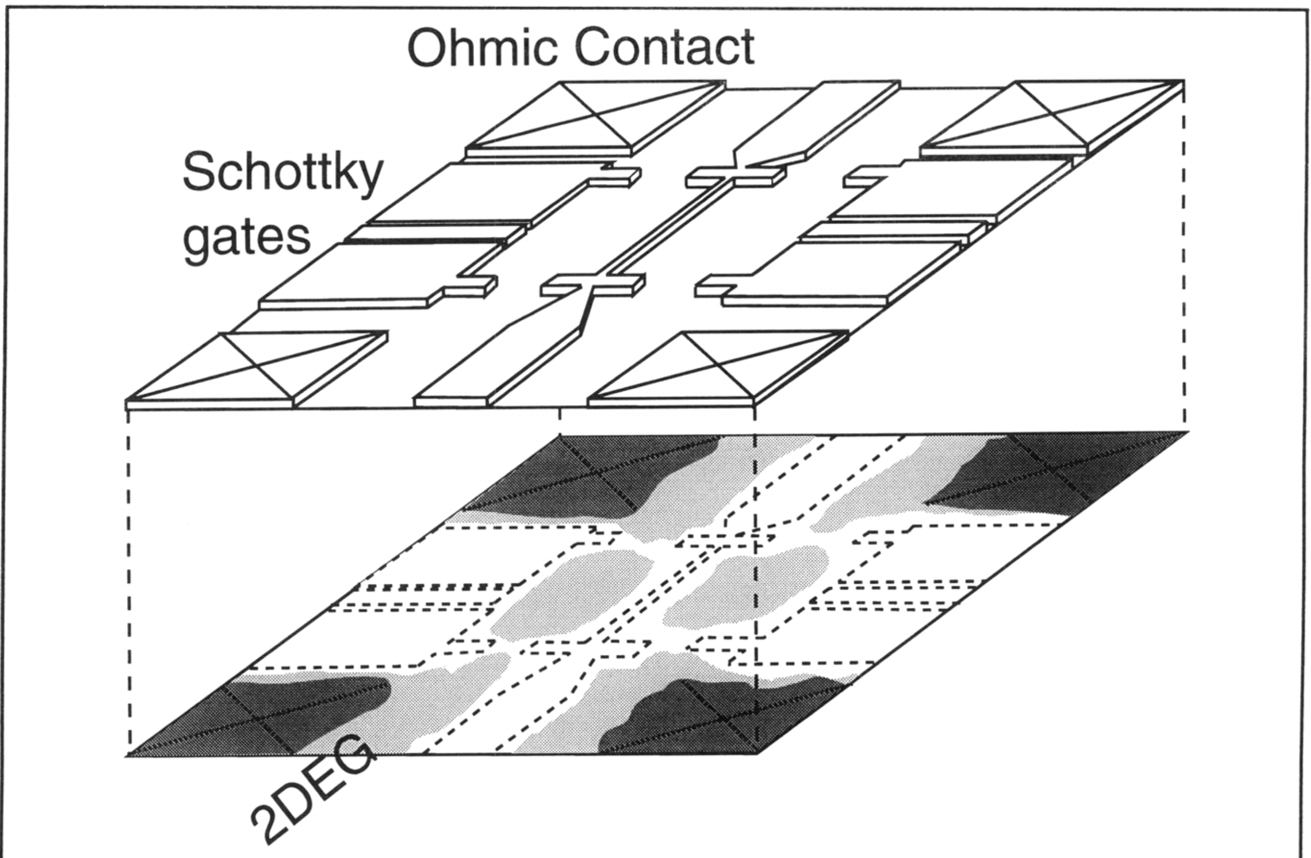

Figure 19. Schematic of a coupled-quantum-dot device. The two-dimensional electron gas (2DEG) is approximately 60 nm below the surface of a GaAs/AlGaAs heterostructure. Ohmic contacts, shown in dark grey, make electrical contact to the 2DEG and Schottky gates on the surface electrostatically create lateral confinement. Regions where the 2DEG exists after biasing the Schottky gates are shown in light grey.

The most critical aspect of quantum dot device fabrication in GaAs heterostructures is the nanolithography. We have been pursuing both direct-write electron-beam lithography and x-ray lithography. X-ray lithography has the advantage of producing more electrostatically robust devices, since thicker resist allows deposition of thicker gate metal and liftoff. It is also more compatible with future manufacturing than is electron-beam lithography.

Figure 20 is a scanning-electron micrograph of the gate structure of a coupled quantum dot device fabricated with electron-beam lithography. Each of the two quantum dots is connected to the outside world via three QPCs. Two QPCs allow tunneling of electrons to the 2DEG reservoirs, and the third QPC allows tunneling between the two dots. This structure will allow investigation of the coupled quantum dots in both parallel and series current flow configurations. We are also investigating devices in which a thin tunnel barrier is formed by a fine line (less than 40 nm) between the two quantum dots instead of by a quantum point contact. (see Section 5.14) We plan to investigate the differences between the two structures as the voltage on the middle Schottky gate is varied and the dots go from being well-separated to being continuous.

We have also designed a one-dimensional quantum-dot-array structure. Figure 21 is a design layout of one of the arrays consisting of seven quantum dots defined by eight quantum point contacts (QPCs). Impurities in the semiconductor strongly affect the characteristics of QPCs. It is essential for our experiments that the tunneling conductance of each QPC in the array be the same. Therefore, each QPC is controlled by a separate voltage source. The device will be fabricated on a back-gated GaAs/AlGaAs heterostructure. The back-gate will allow independent control over the electron density in the 2DEG.

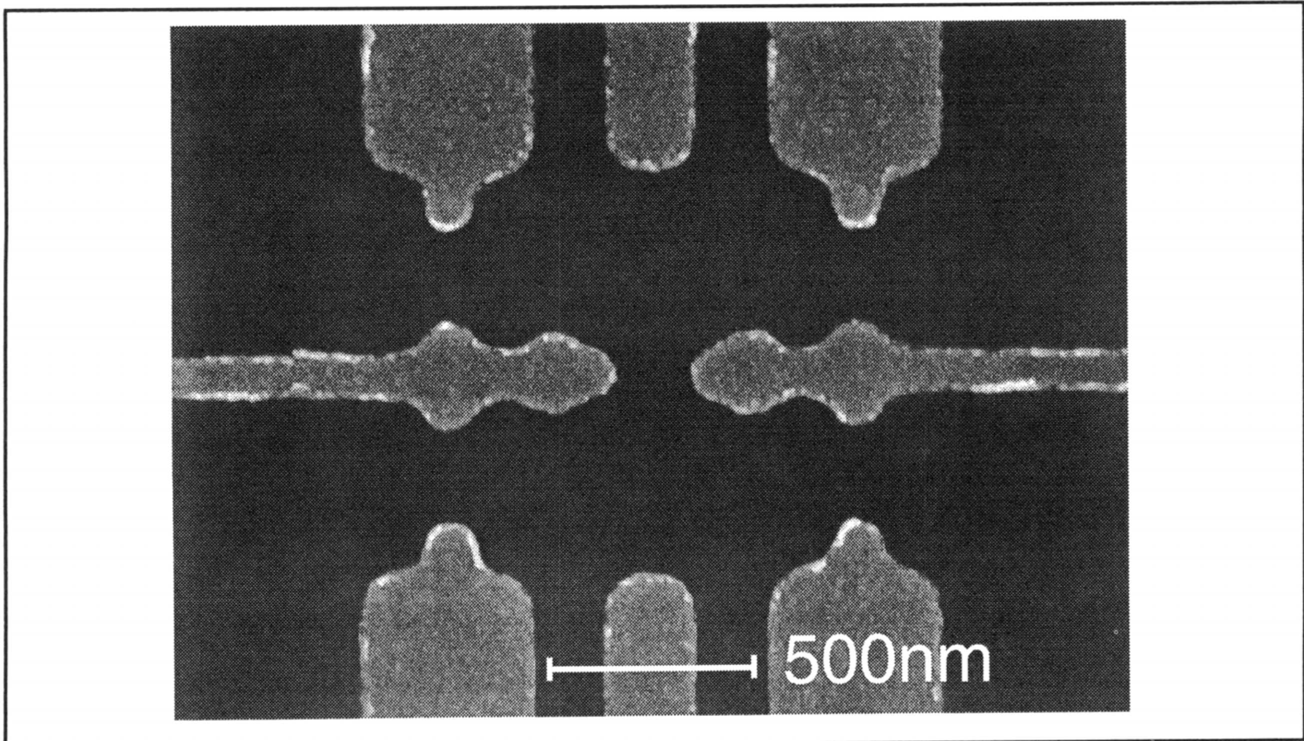

Figure 20. SEM micrograph of a coupled-quantum-dot device on a GaAs/AlGaAs heterostructure, produced by direct-write electron-beam lithography.

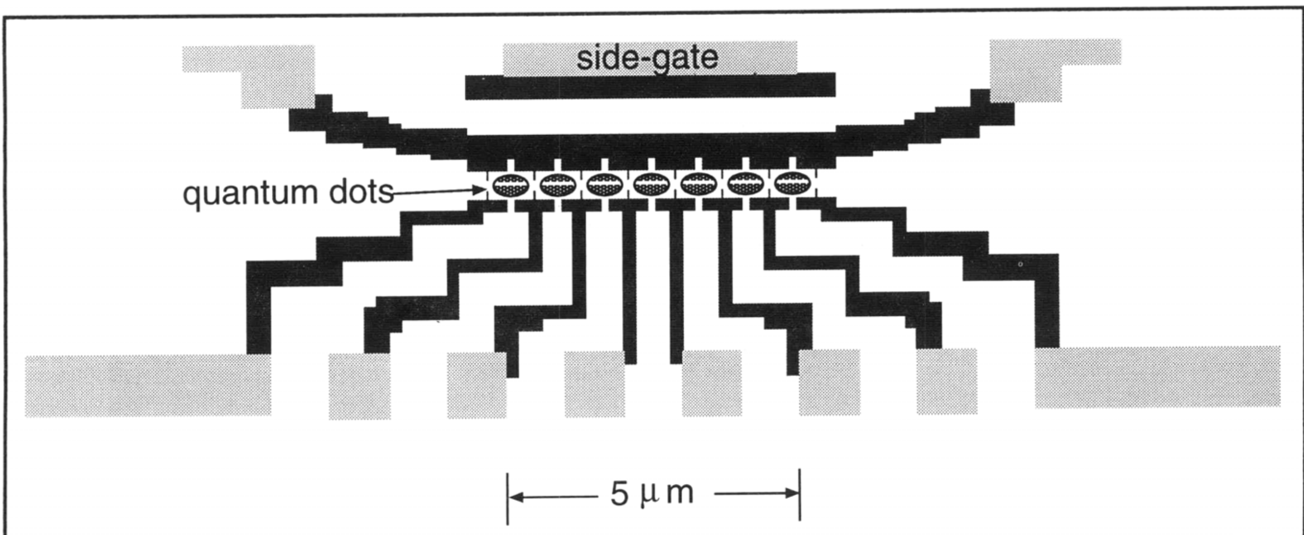

Figure 21. Layout of a series array of seven quantum dots. The eight quantum point contacts are independently controlled to ensure array uniformity.

5.13 Fabrication and Transport Studies of Lateral Surface Superlattices in GaAs/AlGaAs Modulation Doped Field-Effect Transistors

Sponsor

U.S. Air Force- Office of Scientific Research
Grant F-49-620-95-1-0311

Project Staff

Professor Dimitri A. Antoniadis, Michael R. Melloch,[1] Professor Terry P. Orlando, Dr. Anne Pepin, Mark R. Schweizer, Professor Henry I. Smith

Figure 22 depicts a lateral surface superlattice (LSSL) in a GaAs/AlGaAs modulation-doped field-effect transistor (MODFET). When a negative voltage is applied to the gate, the two-dimensional electron gas (2DEG), located at the AlGaAs/GaAs, interface approximately 60 nm under the sample surface, is depleted under the gate fingers. A periodic modulation of the charge concentration is therefore introduced in the 2DEG. As a result, electrons flowing from source to drain are subjected to a two-dimensional superlattice potential (i.e., a two-dimensional array of coupled quantum dots, in the case of the grid-gate shown in figure 22). The strength of the modulation can be adjusted by varying the gate bias.

Evidence of quantum superlattice effect (electron back-diffraction) was clearly observed in 200 nm-period and 60 nm-linewidth grid-gated structures. In the high field regime (high source-to-drain bias), negative differential conductance was also measured in various devices and primarily attributed to sequential resonant tunneling.

Although a wide variety of alternative techniques have since been investigated to induce LSSLs and several studies on magnetotransport measurements in LSSLs have been reported, none of the early transport results obtained at MIT could be reproduced. These objects are of great experimental and theoretical interest, and we have therefore chosen to further investigate electron transport in such structures. New grid-gated and grating-gated GaAs/AlGaAs MODFETs of different periods

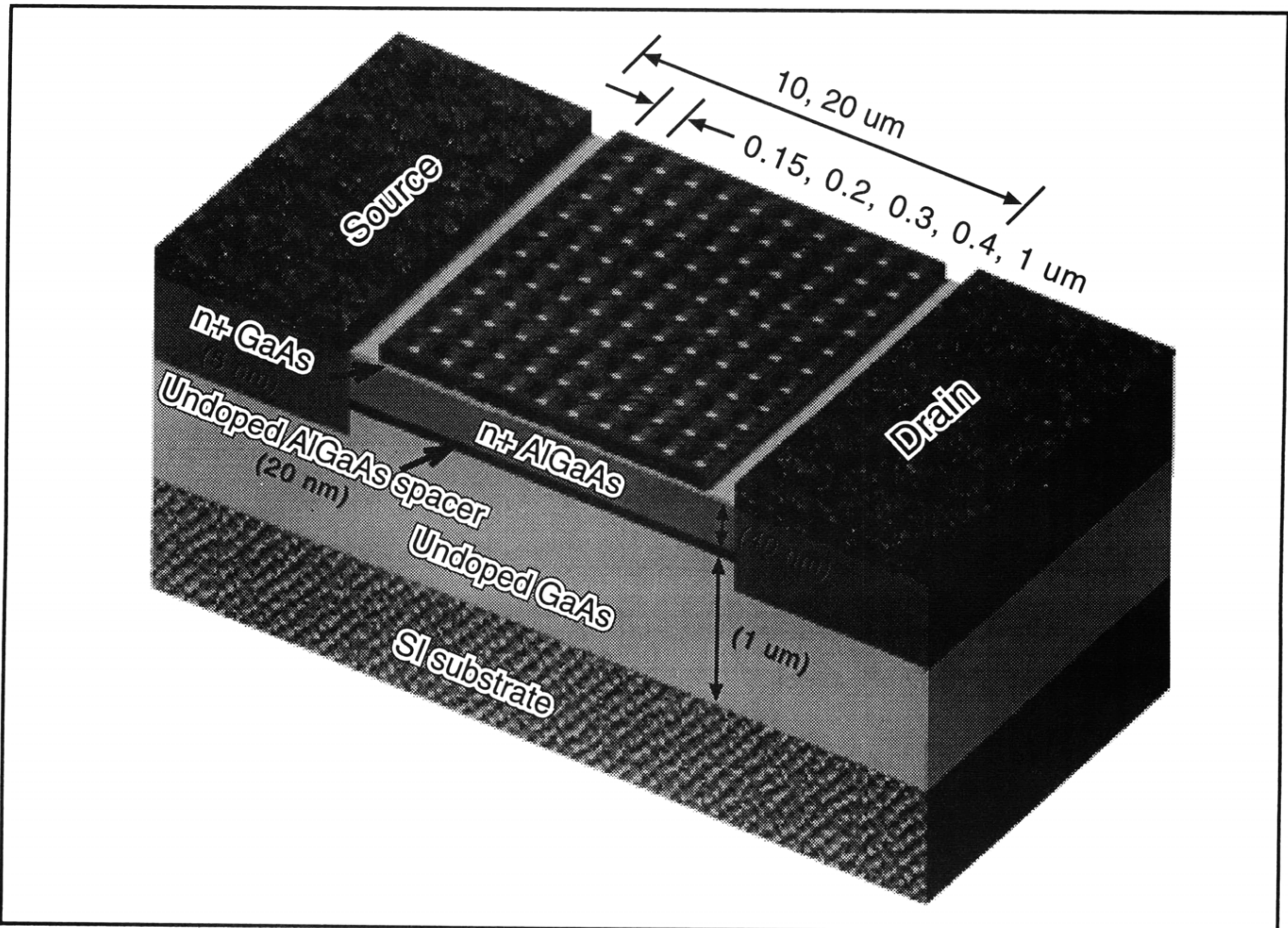

Figure 22. Cross section of the grid-gated MODFET.

(150, 200, 300, 400 nm and 1 μm) and gate lengths (10, 20 μm) are being fabricated. A cross-section of our structure is shown schematically in figure 22. X-ray nanolithography and subsequent metal lift-off are being used to define these structures. Figure 23 displays a scanning electron micrograph of a portion of a 200 nm-period Au grid-gate obtained on an x-ray mask. The gold pattern was obtained on the 1 μm-thick silicon nitride x-ray mask after e-beam nanolithography and subsequent electroplating of 200 nm-thick gold. Linewidths as narrow as 38 nm achieved on x-ray masks should allow us to fabricate high performance devices. Low temperature transport measurement, particularly in the high field regime, will be carried out.

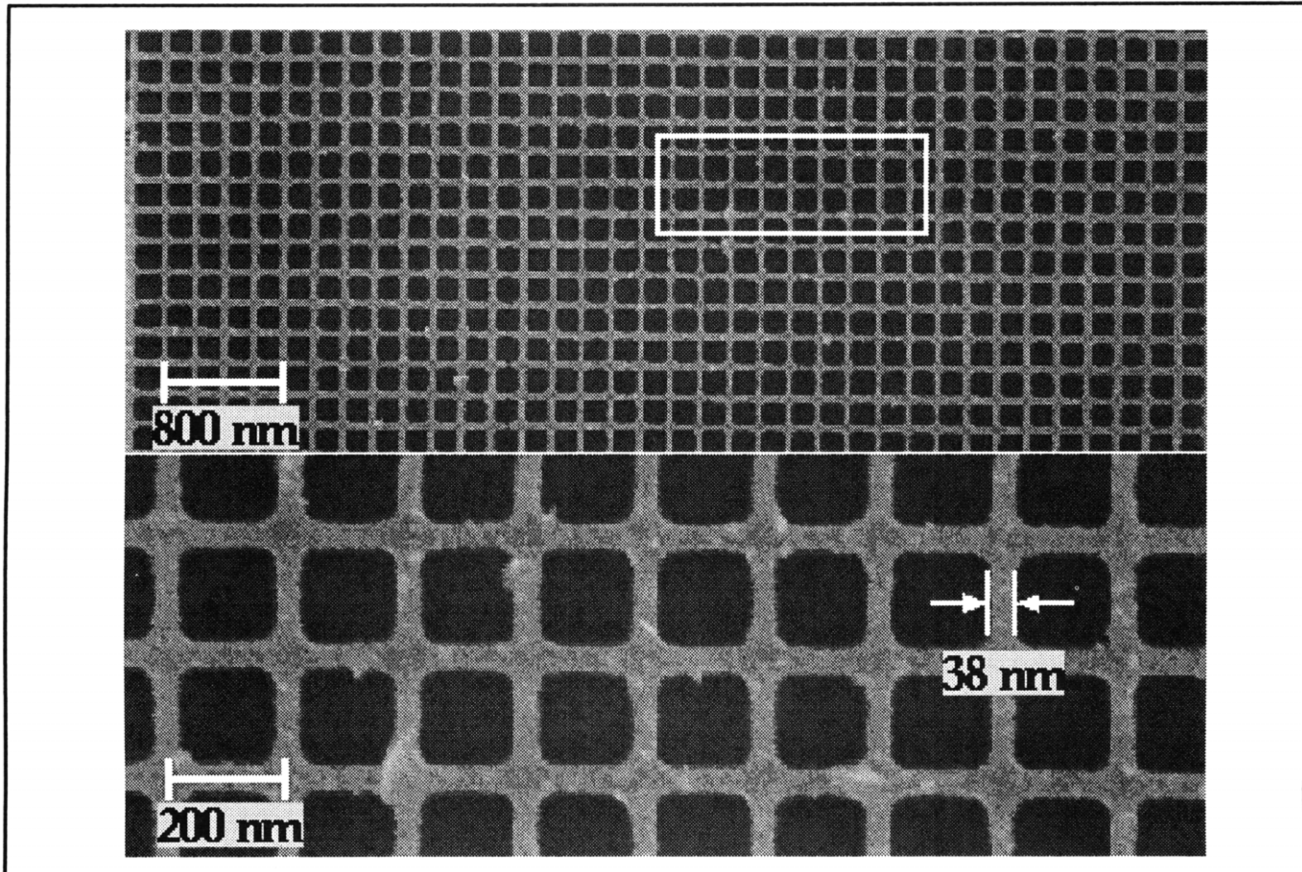

Figure 23. Scanning-electron micrograph of a 200 nm-period and 38 nm-linewidth Au grid-grate obtained on an x-ray mask.

5.14 Single-Electron Transistor Research

Sponsor

Joint Services Electronics Program
Grant DAAH04-95-1-0038

Project Staff

David Berman, Professor Raymond C. Ashoori, Professor Henry I. Smith

The single-electron transistor (SET) has the highest charge sensitivity of any man-made device. In many respects, it is the electrical analog of the SQUID, which is the most sensitive detector of magnetic field. The SET is very well suited for applications where one needs to measure small fluctuations of charge without disturbing the system under study. An example of such a system is a quantum dot.

Figure 24 shows a scanning-electron micrograph of one of our devices. The SET consists of a metal island connected to the source and drain electrodes by two small tunnel junctions. Fabrication of the tunnel junctions is done using a shadow evaporation method.

Operation of the SET depends on the fact that the central island has a very small capacitance, and the energy that it takes for electrons to charge this island is quite large. For example, if the device is cooled to temperatures below 1 K, the electron thermal energy becomes less than the charging

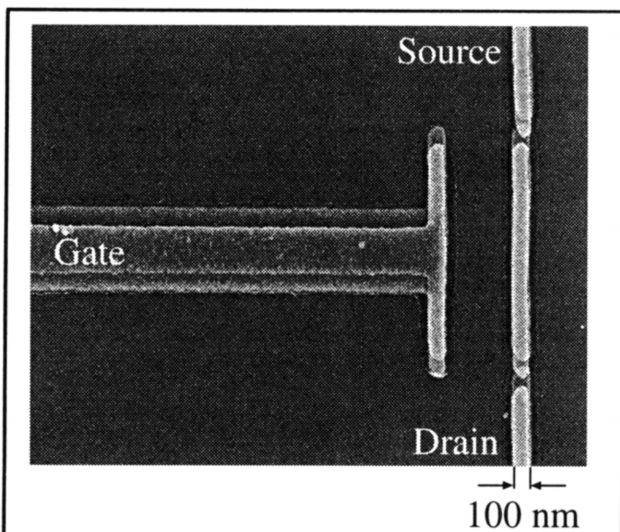

Figure 24. Scanning electron micrograph of a single-electron transistor, made of Al, in which the two tunnel barriers are produced by a two-angle shadow evaporation process.

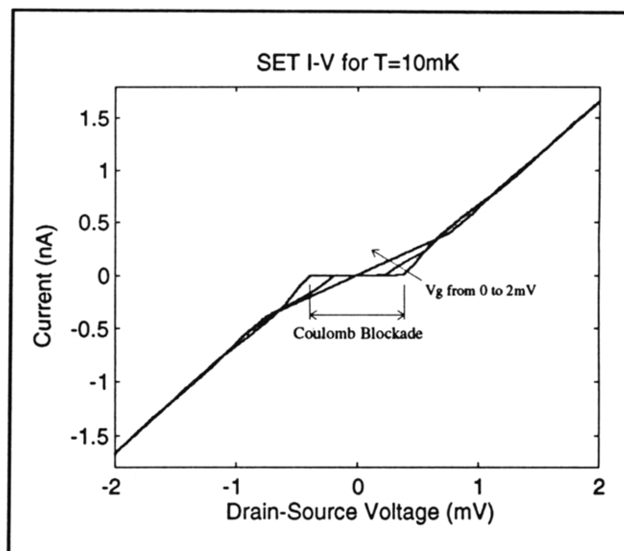

Figure 25. Current-voltage characteristic of a single-electron transistor taken at 10 mK, for three values of gate voltage. The Coulomb blockade is maximum at zero gate bias.

energy. This means that without a significant source-drain voltage bias, the electrons cannot travel through the central island. This effect is known as the Coulomb blockade. The Coulomb blockade is manifested as a zero current region in the current-voltage dependence of the SET. This effect is shown in figure 25. The addition of gate voltage can alter the size of the Coulomb blockade region, thus we can use this device as a transistor.

5.15 Distributed-Feedback Lasers Fabricated by X-Ray Lithography

Sponsors

Joint Services Electronics Program
Grant DAAH04-95-1-0038
U.S. Army Research Office
Grant DAAH04-95-1-0564

Project Staff

Vincent V. Wong, Michael H. Lim, Elisabeth A. Marley, Thomas E. Murphy, James M. Carter, Juan Ferrera, Professor Leslie A. Kolodziejski, Professor Henry I. Smith

Distributed feedback (DFB) lasers are essential components in future wavelength-division-multiplexed systems. These systems require tunable transmitters that oscillate in a single longitudinal mode with narrow linewidths; the transmitters must also be integrable with electronic circuitry such as detectors and field-effect transistors. There are two basic DFB laser structures (figure 26), each with its own fabrication challenges. The fabrication of the vertically-coupled DFB laser requires an epitaxial regrowth step carried out on top of the grating. This etch back step makes the coupling constant after epitaxial regrowth difficult to predict, lowering the yield on these devices. In the laterally-coupled DFB laser structure, gratings are etched on both sides of the ridge waveguide. This structure eliminates the need for regrowth and maximizes the utility of ridge-waveguide devices.

To achieve high enough contra-directional coupling for laser action to occur in the laterally-coupled DFB structure, as well as reliable control of coupling from device-to-device, the lateral gratings should run right up to the ridge sidewall since the coupling decreases as the lateral gratings move away from the ridge sidewall. This decrease is attributable to the decreased overlap between the optical field and the grating. For reasonable values of k ($\sim 20\ cm^{-1}$), the lateral gratings must be within 100 nm of the ridge sidewall. Lateral gratings that reside closer to the ridge sidewall also relax the tolerance on the grating duty cycle. However, spinning a thin coat of resist onto a wafer with a high ridge-waveguide results in a buildup next to the sidewall of the ridge; at thicknesses of greater than 1 mm this poses problems even for x-ray lithography. This buildup of resist prevents the gratings from running all the way up to the ridge sidewall.

We have developed a process, that uses ion implantation (figure 27) to overcome this problem. Once the ridge waveguides are defined, a 4.3 μm-thick planarizing layer of PMMA is spun onto the substrate. Next, three ion implantation/development steps are performed: (1) boron

700 keV; 10^{13} cm^{-2}; 1:2 MIBK:IPA at 21° C for 150 seconds; (2) boron 120 keV; 10^{13} cm^{-2}; 1:2 MIBK:IPA at 21° C for 150 seconds; (3) boron 80 keV; 10^{13} cm^{-2}; 1:2 MIBK:IPA at 21° C for 150 seconds. After these steps, a 0.6 μm film of PMMA remains. Into this film, x-ray lithography defines a uniform 406 nm-period grating that runs up to the ridge waveguide sidewalls. The grating is then etched in a CH_4/H_2 plasma. Figure 28 shows the results, lateral gratings that run right up to the edge of the ridge-waveguide.

The challenges of fabricating high quality vertically-coupled DFB laser are quite different than those of a laterally coupled DFB laser. Because of the geometries of the VC-DFB, high quality regrowth on a grating is the primary concern. In 1996, we will investigate such regrowth as a function of grating aspect ratio.

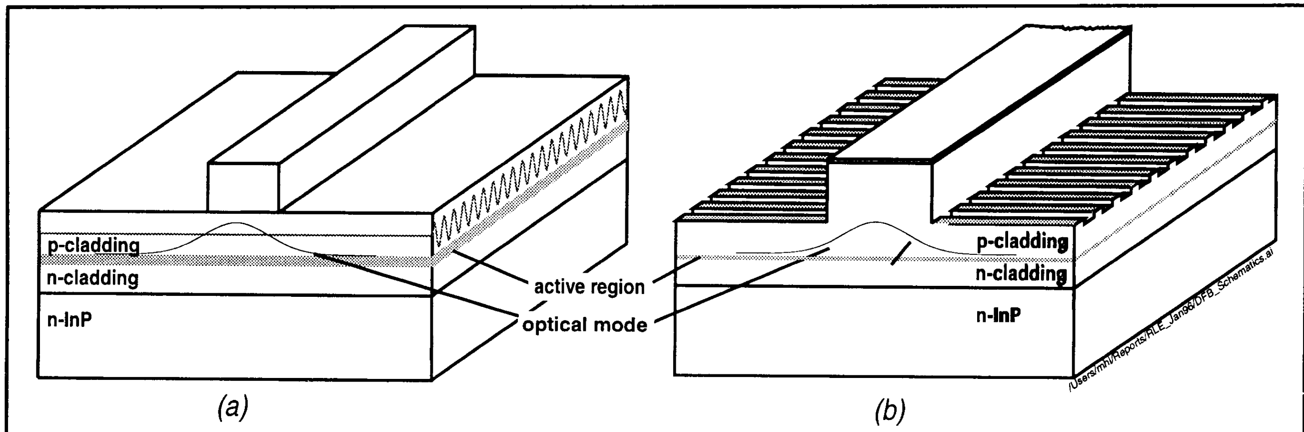

Figure 26. (a) A schematic of a DFB laser that relies on coupling vertically to the corrugation region above the gain region; (b) schematic of a laterally-coupled DFB laser that relies on coupling laterally to the corrugation regions on the side of the ridge waveguide. For adequate contra-directional coupling to occur, the distance from the sidewall of the ridge to the beginning of the grating must be less than 100 nm.

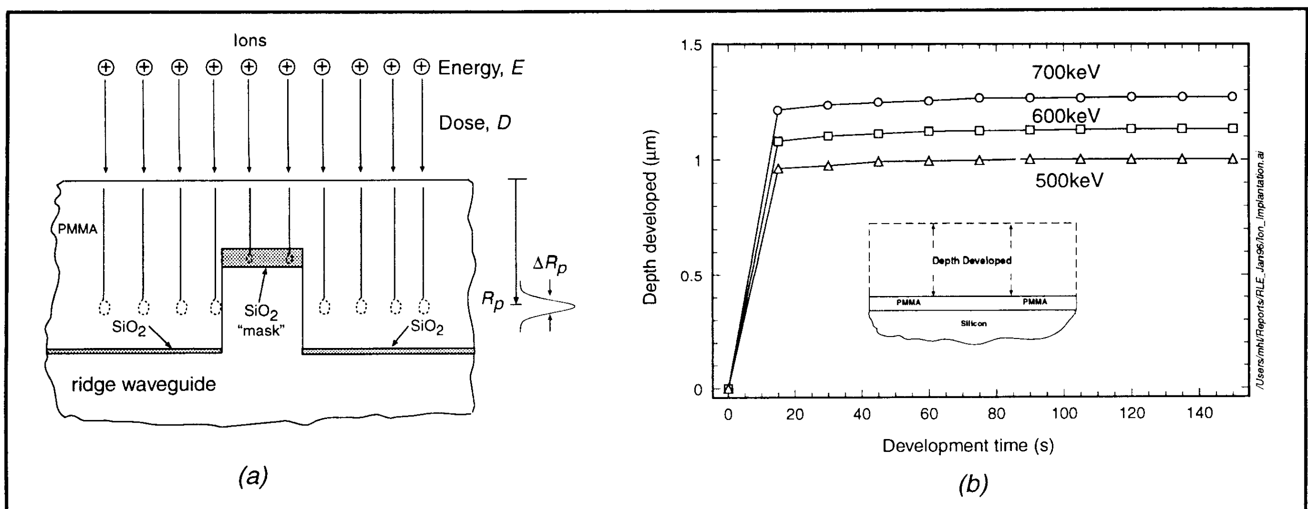

Figure 27. (a) When high energy ions are implanted, the majority of the ions stop at a particular depth governed by the energy of the ion. This allows one to develop the thick PMMA down to a thin film for x-ray exposure; (b) the depth of the developed PMMA saturates at a particular depth dependent on the energy of the implanted ion. The ion dose was 1x 10^{13} cm^{-2}. The PMMA was developed in a solution of 1:2 MIBK:IPA at 21° C.

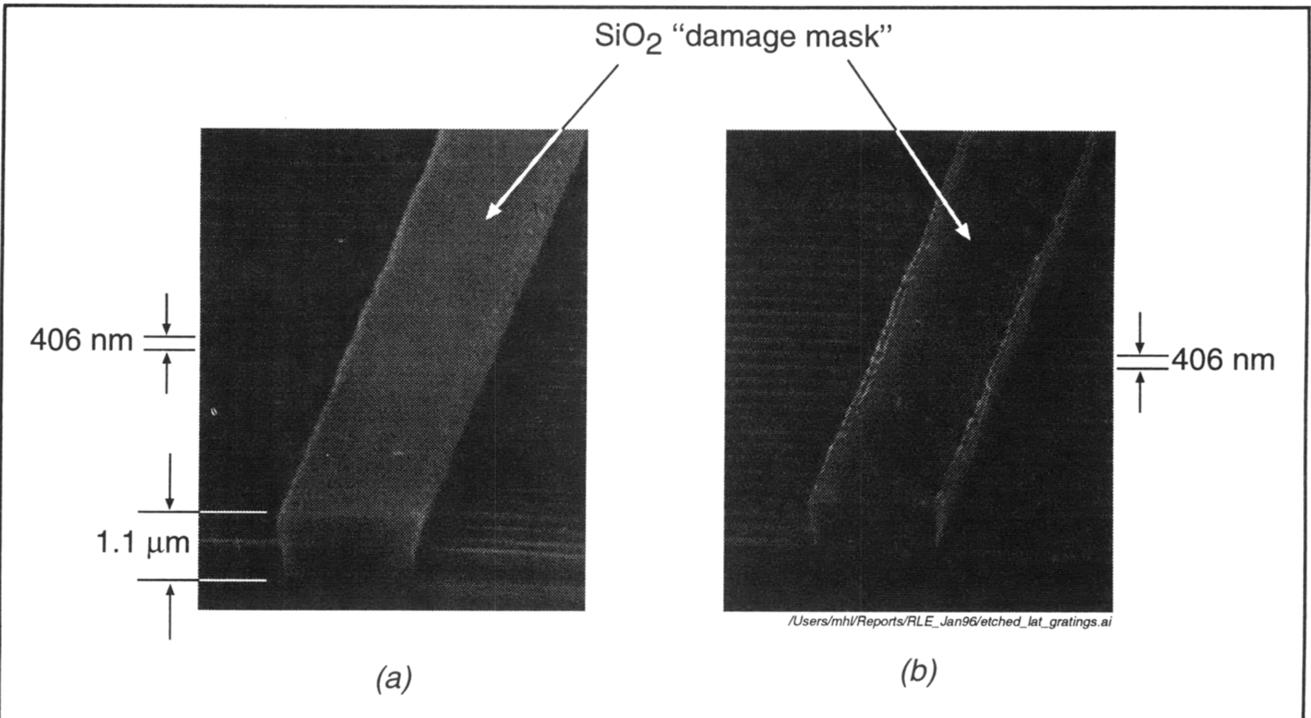

Figure 28. Lateral gratings defined on a 1.1 μm-high InP/InGaAlAs/InGaAsP ridge-waveguide. The grating has a period of 406 nm, which corresponds to a 2nd-order DFB laser operating at 1.3 μm wavelength. The silicon dioxide damage mask serves both as an RIE etch mask as well as an ion implantation damage mask. (a) scanning electron micrograph of a 406 nm-period lateral grating exposed in PMMA by x-ray lithography; (b) scanning electron micrograph of lateral gratings defined by CH_4/H_2 RIE.

5.16 Fabrication of Integrated Quarter-Wave Shifted Distributed Bragg Gratings for Wavelength Division Multiplexing Applications

Sponsor

Joint Services Electronics Program
Grant DAAH04-95-1-0038

Project Staff

Jay N. Damask, Juan Ferrera, Michael H. Lim, Thomas E. Murphy, Vincent V. Wong, Professor Hermann A. Haus, Professor Henry I. Smith

In order to best utilize the bandwidth available for optical communications systems, it is advantageous to transmit several communications signals in a single optical fiber, each modulated with a different carrier frequency. One key component in the implementation of such wavelength division multiplexed (WDM) systems is a narrow-band optical filter that can separate or "drop" one channel from a waveguide, leaving the other channels undisturbed.

Quarter-wave shifted Bragg gratings provide a compact, flexible filter for WDM applications. Insertion of an abrupt quarter-wave shift in an otherwise coherent distributed Bragg grating gives rise to a single narrow resonance at the Bragg wavelength. The small spatial periods required for these grating filters (~510 nm in SiO_2 materials and ~250 nm in InP materials) necessitates the use of advanced nanolithography techniques in their fabrication.

The integrated resonant channel dropping filter (figure 29) is comprised of two quarter-wave shifted gratings, each evanescently side-coupled to a bus waveguide. The function of the filter is to spatially separate, or drop, just one channel from the bus waveguide without terminating or otherwise disturbing the remaining channels. The WDM bitstream is carried along the middle waveguide. Only that channel, or wavelength band, that excites the side-coupled resonators is removed from the bus to the upper waveguide. The remaining channels travel through undisturbed.

The Lorentzian filter response of a quarter-wave shifted grating is limited to a filter roll-off of -10 dB/decade away from the resonant frequency. In order to improve the filter roll-off, several such resonators can be cascaded along a single waveguide, producing a so-called multiple-pole filter, as shown in figure 30.

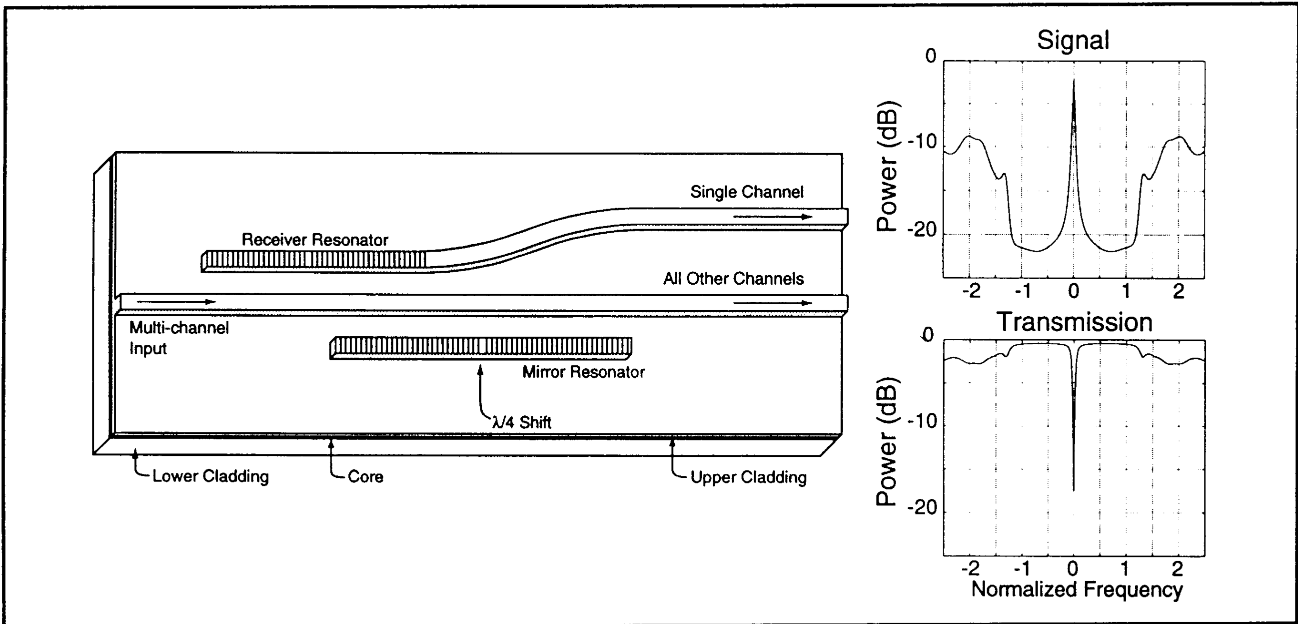

Figure 29. A schematic diagram of the integrated resonant channel-dropping filter, and the associated filter spectral response.

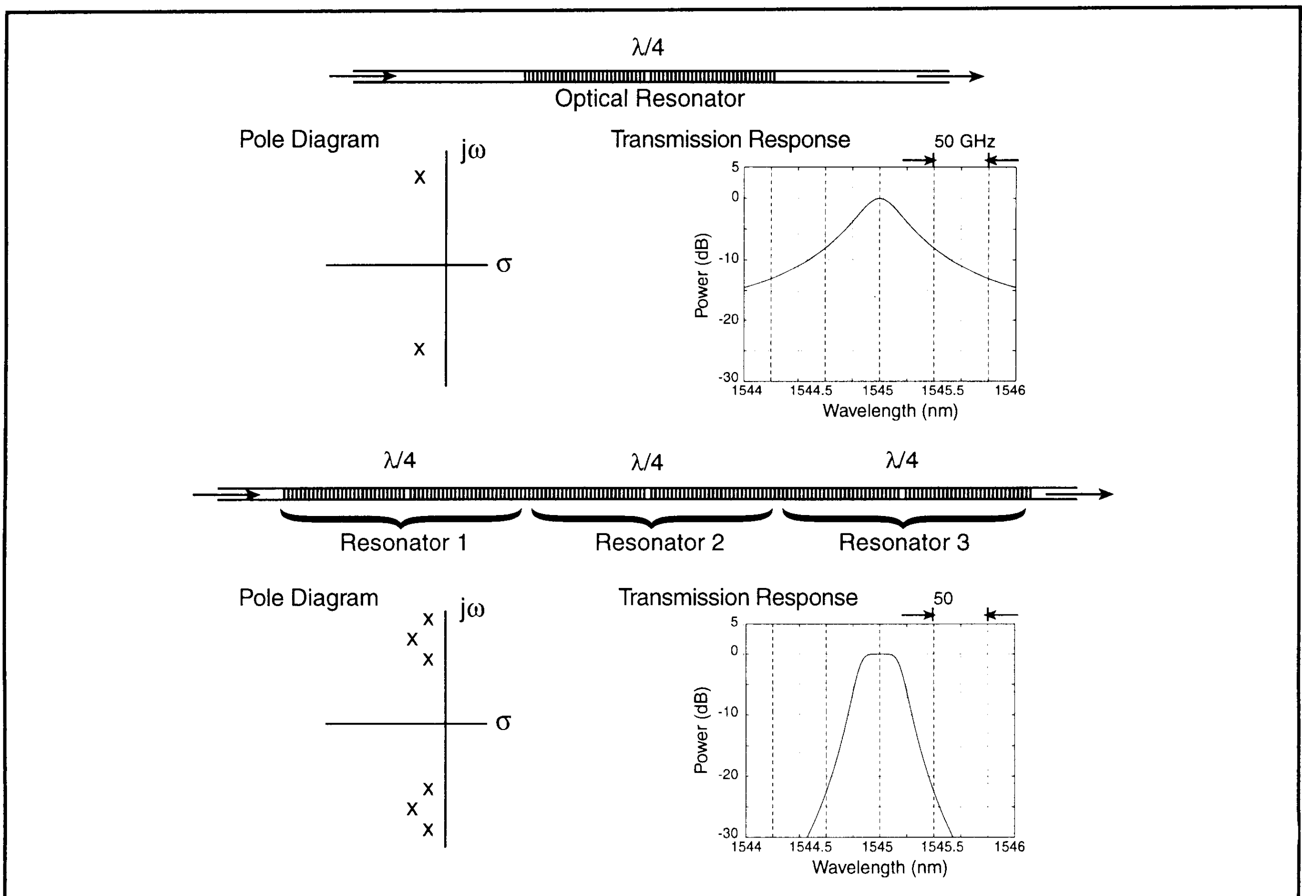

Figure 30. A comparison of the response of a single-pole Lorentzian filter to that of a properly designed multiple-pole filter.

We are developing the techniques to design and fabricate integrated resonant channel-dropping filters and higher-order cascaded quarter-wave shifted Bragg filters. We describe here our progress towards this goal, which includes the design of quarter-wave shifted filters, device fabrication using a combination of spatial-phase-locked e-beam, optical and x-ray lithographies, and finally device measurement and characterization.

The initial waveguide geometry consists of a 4 mm thick SiO_2 lower cladding layer, a 154 nm thick Si_3N_4 core region, topped by another SiO_2 cladding layer of thickness 340 nm. The guiding structure was constructed by optical lithography and reactive ion etching of the top cladding region to form a rib waveguide. After reactive-ion etching, chromium was deposited and a liftoff step performed, resulting in a layer of chromium covering all but the top of the rib waveguide. This layer of chrome acts as an etch mask in subsequent processing of the Bragg gratings, thereby ensuring that the gratings reside only on the top of the rib.

Fabrication of coherent quarter-wave-shifted gratings presents challenges to conventional lithography techniques. While long coherent gratings can be generated using interferometric lithography, quarter-wave-shifted gratings require the use of electron beam lithography (EBL). Since the grating lengths required by these types of filters extend beyond one EBL field, the grating patterns must be composed by stitching together several fields. In order to eliminate interfield stitching errors, which can ruin the coherence of the grating and adversely effect the filter performance, spatial phase locked e-beam lithography (SPLEBL) is used to pattern the gratings. To increase the throughput of the fabrication process, making the device more commercially viable, the gratings are e-beam written only once onto an x-ray mask, which is subsequently used to transfer the gratings to the waveguides.

The chemically amplified positive resist, ESCAP, was used for patterning of the Bragg gratings with x-ray lithography. An alignment step was necessary to place the gratings on the optical waveguides with the correct orientation and at the correct position. Note, however that because the chrome mask automatically confines the gratings to the tops of the rib waveguides, alignment of the gratings in the lateral direction is not critical, provided that the grating patterns are wide enough to cover the waveguides.

The gratings were etched to a target depth of 150 nm using reactive ion etching. In order to achieve a high degree of control for the grating etch depth, a two step etching technique was developed in which the sample is measured at an intermediate point during the etch process to determine the etching rate.

Figure 31 shows the optical transmission response of a single-pole filter, consisting of a quarter-wave shifted grating which spans nine e-beam fields. Figure 32 presents the optical transmission measurements of first-, third-, fifth-, and seventh-order Gaussian mutiple pole filters, consisting of one or more cascaded quarter-wave shifted Bragg resonators fabricated by the methods described above. The 0.1 nm resolution of the spectrum analyzer used for the measurements limits the degree to which we can measure the filter roll-off as the filter order is increased.

Our continuing work in this area includes the design and fabrication of more complex device structures such as side-coupled resonators and ultimately integrated channel-dropping filters. We are also investigating other grating based devices such as apodized grating filters where the grating strength varies continuously along the length of the grating. Such devices are predicted to have very low sidelobe levels compared to conventional gratings. Additionally, we plan to construct grating based devices in the InP/InGaAsP material system, in the process investigating and developing techniques for reliably regrowing high quality material over etched grating regions.

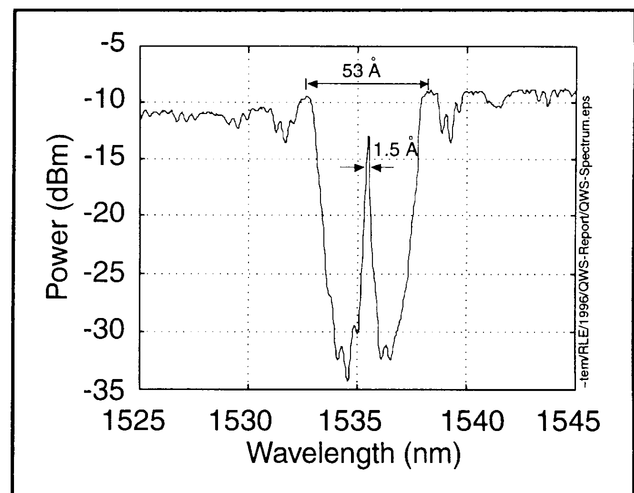

Figure 31. Measured optical transmission response of a single-pole quarter-wave shifted Bragg grating, spanning nine e-beam lithography fields.

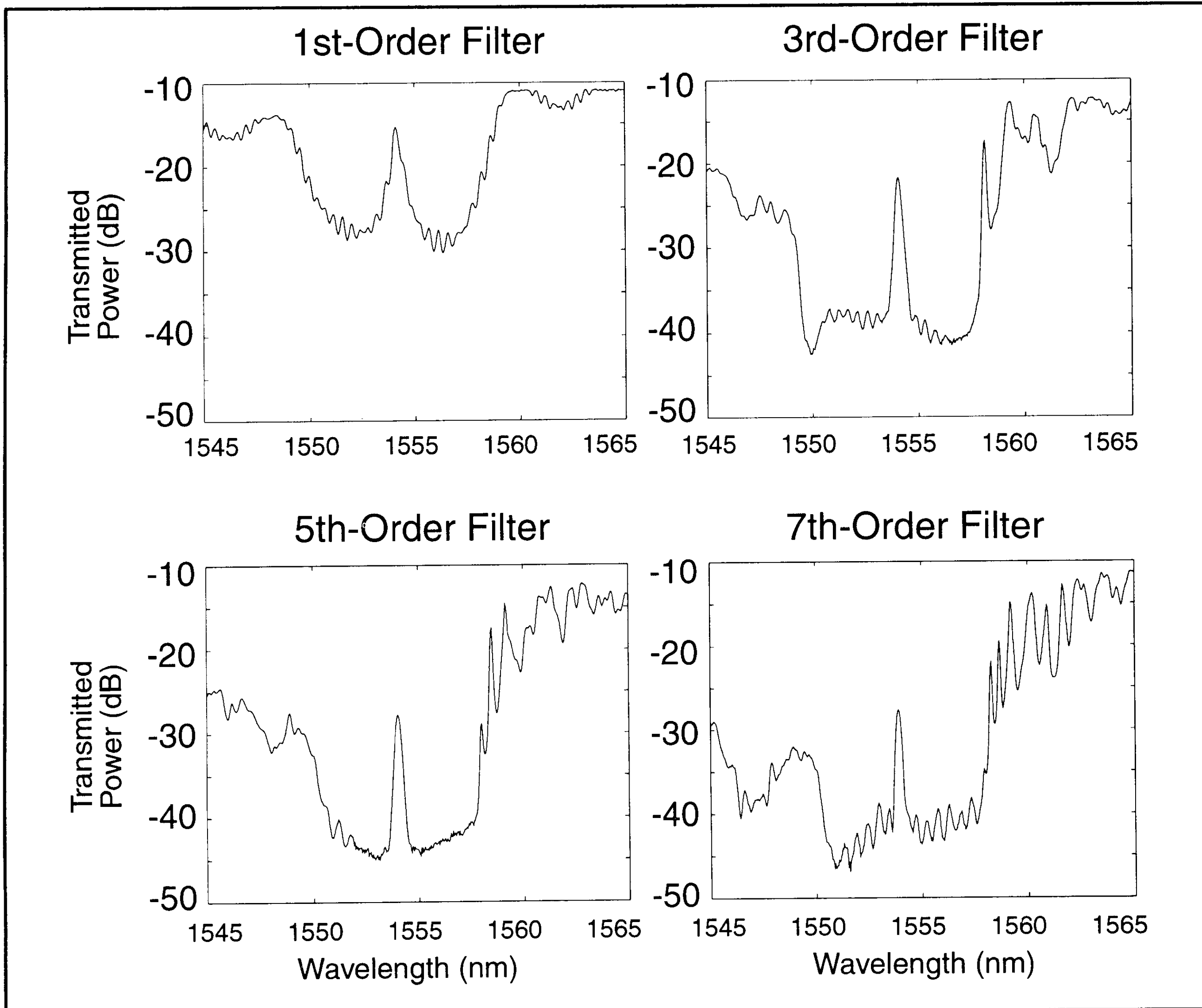

Figure 32. Measured optical transmission response of first-, third-, fifth-, and seventh-order Gaussian mutiple pole filters. The shape of the filter response near resonance is not well resolved by the optical spectrum analyzer, but the sidelobes on the long-wavelength side are indicative of a Gaussian multiple-pole filter response.

5.17 Design of a Grating-Based Matched Filter for Optical Communications

Sponsor

Joint Services Electronics Program
Grant DAAH04-95-1-0038

Project Staff

Jay N. Damask, Thomas E. Murphy, Professor Hermann A. Haus, Professor Henry I. Smith

In any long-distance optical-communications system, broadband noise is introduced during optical amplification. Optical filters are needed to improve the signal-to-noise ratio before the amplified signal is detected. The optimal filter is one that matches the spectrum of the original noise-free signal. Such a matched filter gives the largest possible signal-to-noise ratio when the filtered signal is sampled.

Figure 33 depicts a typical 10 Gb/s optical signal, consisting of a sequence of square pulses 100 ps in duration, each representing a single bit. The corresponding signal spectrum has the characteristic $\sin(\Delta\omega T)/\Delta\omega T$ shape, centered at the optical carrier wavelength of 1.55 μm.

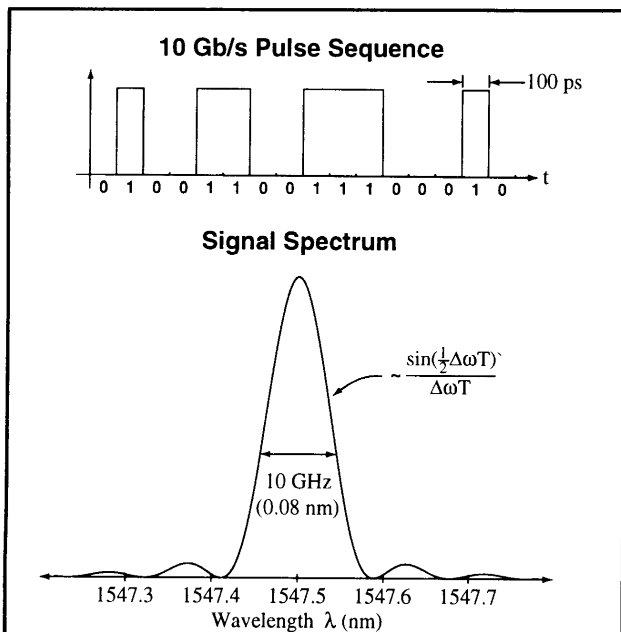

Figure 33. A typical 10 Gb/s binary encoded optical signal, and the corresponding signal spectrum. Note that only the slow 10 Ghz amplitude modulation is depicted in the pulse diagram. The rapid oscillations associated with optical carrier frequency are not shown.

The reflection spectral response of a properly designed weak Bragg grating can match the spectrum of the incident pulse stream, thereby providing a convenient way to realize a matched filter. In order for the grating to have the desired spectral width, the grating length must be chosen such that the down and back propagation time of light in the grating is equal to one pulse duration. For SiO_2-based waveguides, this corresponds to a grating length of ~1 cm. In order for the grating spectrum to be centered at a free-space wavelength of 1.55 μm (commonly used in optical communications), the period of the Bragg grating must be approximately 530 nm.

The weak grating filter operates as a single pass filter where the grating reflects a small portion of the signal back into the input port. The reflection spectrum of the weak grating has the same $\mathrm{sinc}(\Delta\omega T)$ shape as an incident pulse stream. However, this response comes at the expense of a decreased power return, because much of the incident signal passes through the grating without being reflected. If the grating is made stronger, to try to increase the power return, the response no longer resembles a sinc function but rather has a characteristic plateau response associated with a strong Bragg grating.

Figure 34 depicts a weak Bragg grating filter, constructed in a Mach-Zehnder interferometer. The Mach-Zehnder configuration provides a means of spatially separating the reflected signal from the input signal. In this device, two identical grating filters are placed in opposite arms of a Mach-Zehnder interferometer. Light is launched in the upper port of the device and a codirectional coupling region transfers half of the signal to the lower waveguide. A portion of the light in each arm of the interferometer is reflected by the two identical weak gratings. The reflected signals recombine in the 50 percent coupling region and emerge in the lower port of the device.

Because one function of the device is to filter out broadband noise introduced during optical amplification, it is counterproductive to reamplify the filtered signal, as this would only reintroduce noise. Consequently, it is important to minimize the total insertion loss of the device. Sources of loss include material loss, bending-induced loss, and fiber-coupling loss. In design of the device, we have investigated each of these loss factors in an attempt to minimize the total insertion loss without compromising the device performance.

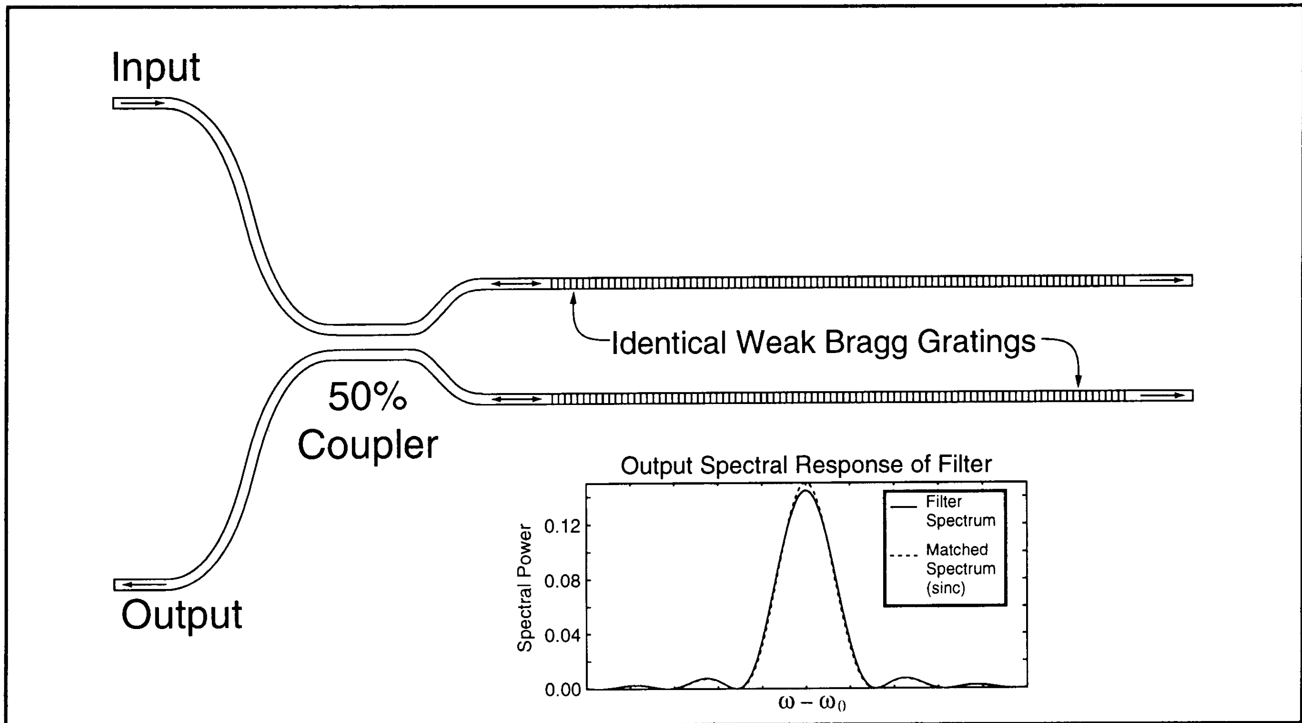

Figure 34. Two identical weak Bragg gratings, constructed in a Mach-Zehnder configuration. The Mach-Zehnder configuration provides spatial separation of the input signal and the filtered signal.

The waveguides will be fabricated from commercially available Ge doped SiO_2 slab waveguides. This material system has been shown to have low material loss, and favorable device dimensions. Because the index of refraction of SiO_2 is comparable to that found in most optical fibers, the device allows for good fiber coupling. Additionally, Ge doped SiO_2 has been shown to have photorefractive properties: irradiating the Ge doped core region with UV light can induce a small, permanent index change in the material. This effect could be used to adjust the relative phase between the two arms of the interferometer.

We plan to use optical lithography and reactive ion etching to construct the optical waveguides for this device. Interferometric lithography will be used to generate the long, spatially coherent gratings on an x-ray mask. The grating patterns can then be transferred to the waveguides using x-ray lithography, and reactive ion etched to form the grating corrugations.

We have completed the design of these filters and are presently fabricating them. The technologies required to build these filters should prove useful in the future for design and fabrication of related grating based devices, such as strong-grating filters and apodized grating filters, which could find important applications in wavelength division multiplexing.

5.18 High-Dispersion, High-Efficiency Transmission Gratings for Astrophysical X-ray Spectroscopy

Sponsor

National Aeronautics and Space Administration
Contract NAS8-38249
Grant NAGW-2003

Project Staff

Richard J. Aucoin, Robert C. Fleming, Dr. Mark L. Schattenburg, Professor Claude R. Canizares, Professor Henry I. Smith

Through a collaboration between the Center for Space Research (CSR) and the Nanostructures Laboratory (NSL), transmission gratings are provided for the Advanced X-ray Astrophysics Facility (AXAF) x-ray telescope, scheduled for launch on the NASA Space Shuttle in 1998. Many hundreds of large area, gold transmission gratings of 200 nm and 400 nm periods are required. In order to achieve spectrometer performance goals, the gratings need to have very low distortion. The gratings will provide high resolution x-ray spectroscopy of astrophysical sources in the 100 eV to 10 keV band.

The need for high grating quality and an aggressive production schedule require the development of a robust, high-yield manufacturing process. We have adopted a scheme involving interference lithography with tri-level resist, followed by cyrogenic reactive-ion etching and gold electroplating. A chemical etching step then yields membrane-supported gratings suitable for space use. The gratings undergo extensive testing before being released for use in the spectrometer.

The Space Microstructures Laboratory, a new cleanroom fabrication facility, on the fourth floor of Building 37 (adjacent to the Gordon Stanley Brown Building) has been constructed in order to fabricate AXAF gratings. The proximity of the new lab to the Microsystems Technology Laboratory (MTL) has allowed the lab to share many MTL services such as DI and process water, nitrogen, process vacuum, and waste drains. The laboratory space includes 1700 square feet of Class 100 and associated support areas. Production of flight gratings is underway.

5.19 Submicrometer-Period Transmission Gratings for X-ray and Atom-Beam Spectroscopy and Interferometry

Sponsors

Joint Services Electronics Program
Grant DAAH04-95-1-0038
National Aeronautics and Space Administration
Contract NAS8-38249
Grant NAGW-2003

Project Staff

James M. Carter, Jeanne M. Porter, Timothy A. Savas, Dr. Mark L. Schattenburg, Professor Henry I. Smith

Transmission gratings with periods of 100-1000 nm are finding increasing utility in applications such as x-ray, vacuum-ultraviolet, and atom-beam spectroscopy and interferometry. Over 20 laboratories around the world depend on MIT-supplied gratings in their work. For x-ray and VUV spectroscopy, gratings are made of gold and have periods of 100-1000 nm and thicknesses ranging from 100-1000 nm. They are most commonly used for spectroscopy of the x-ray emission from high-temperature plasmas. Transmission gratings are supported on thin (1 μm) polyimide membranes or made self supporting ("free standing") by the addition of crossing struts (mesh). For short x-ray wavelengths membrane support is desired, while for the long wavelengths a mesh support is preferred in order to increase efficiency. Fabrication is performed by interferometric lithography combined with reactive-ion etching and electroplating. Progress in this area tends to focus on improving the yield and flexibility of the fabrication procedures.

Another application is the diffraction of neutral atom and molecular beams by mesh supported gratings. Lithographic and etching procedures have been developed for fabricating free-standing gratings in thin silicon nitride (SiN_x) supported in a Si frame. Figure 35 shows a free-standing 100 nm period grating in 1000 Å-thick silicon nitride.

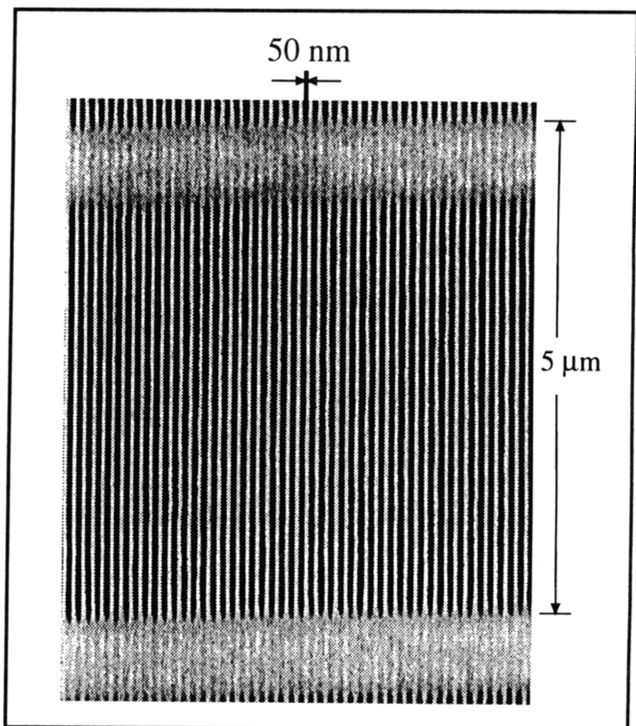

Figure 35. Scanning electron micrograph of a free-standing 100 nm period grating in a silicon nitride membrane of area 500 μm by 5 mm.

We have established a collaboration with the Max Planck Institute in Goettingen, Germany which will utilize our gratings of 100 nm period in diffraction and interferometer experiments using He atom beams.

5.20 Publications

5.20.1 Journal Articles

Aucoin, R.J., and M.L. Schattenburg. "Optically-Matched Tri-Level Resist Process for Nanostructure Fabrication." *J. Vac. Sci. Technol. B* 13: 3007-3011 (1995).

Grayson, M., D.C. Tsui, and M. Shayegan. "Far-infrared Emission from Hot Quasi-One-Dimensional Quantum Wires in GaAs." *Appl. Phys. Lett.* 67: 1564 (1995).

Moon, E.E., P.N. Everett, and H.I. Smith. "Immunity to Signal Degradation by Overlayers Using a Novel Spatial-Phase-Matching Alignment System." *J. Vac. Sci. Technol. B* 13: 2648-2652 (1995).

Savas, T.A., S.N. Shah, M.L. Schattenburg, J.M. Carter, and H.I. Smith. "Achromatic-Interferometric Lithography for 100 nm-Period Gratings and Grids." *J. Vac. Sci. Technol. B* 13: 2732-2735 (1995).

Smith, H.I. "100 Years of X-rays: Impact on Micro- and Nanofabrication." *J. Vac. Sci. Technol. B* 13: 2323-2328 (1995).

Smith, H.I. "X-ray Lithography for Microelectronics." Jubilee Symposium, *X-rays in Natural Science and Medicine,* Uppsala University, Sweden, March 23-24 1995; *Physica Scripta*. Forthcoming.

Smith, H.I., M.L. Schattenburg, S.D. Hector, J. Ferrera, E.E. Moon, I.Y. Yang, and M. Burkhardt. "X-ray Nanolithography: Extension to the Limits of the Lithographic Process." *Nanotechnology*, Special Issue of *Microelectron. Eng.* Forthcoming.

Wong, V.V., A. Yasaka, and H.I. Smith. "Resist Planarization over Topography using Ion Implantation." *J. Vac. Sci. Technol. B* 13: 2797-2800 (1995).

Wong, V.V., J. Ferrera, J.N. Damask, T.E. Murphy, and H.I. Smith. "Distributed Bragg Grating Integrated Optical Filters; Synthesis and Fabrication." *J. Vac. Sci. Technol. B* 13: 2859-2864 (1995).

Yang, I.Y., J.M. Carter, S.E. Silverman, S. Rishton, D.A. Antoniadis, and H.I. Smith. "Combining and Matching Optical, E-beam and X-ray Lithographies in the Fabrication of Si CMOS Circuits with 0.1 and Sub-0.1 μm Features." *J. Vac. Sci. Technol. B* 13: 2741-2744 (1995).

Zhao, Y., D.C. Tsui, M.B. Santos, and M. Shayegan. "Grating-Induced Cyclotron-Resonance Anomaly in GaAs/$Al_1Ga_{1-x}As$ Heterostructures." *Phys. Rev. B* 51: 174 (1995).

5.20.2 Conference Proceedings

Burkhardt, M., S. Silverman, H.I. Smith, D.A. Antoniadis, K.W. Rhee, and M.C. Peckerar. "Gap Control in the Fabrication of Quantum-Effect Devices Using X-Ray Nanolithography." *Microelectron. Eng.* 27: 307-310 (1995).

Choi, W.-Y, V.V. Wong, J.C. Chen, H.I. Smith, and C.G. Fonstad. "Design and Fabrication using X-Ray Lithography of Ridge-Waveguide Distributed Feedback Structures on InP." *International Conference on InP and Related Compounds*, Santa Barbara, California March 1994.

Ferrera, J., M.L. Schattenburg, and H.I. Smith. "Analysis of Distortion in Interferometric Lithography." Submitted to *40th International Symposium on Electron Ion and Photon Beam Technology and Nanofabrication.*

Moon, E.E., P.N. Everett, and H.I. Smith. "Simultaneous Measurement of Gap and Superposition in a Precision Aligner for X-ray Nanolithography." Submitted to *40th International Symposium on Electron Ion and Photon Beam Technology and Nanofabrication.*

Rooks, M.J., R.C. Tiberio, M. Chapman, T. Hammond, E. Smith, A. Lenef, R. Rubenstein, D. Pritchard, S. Adams, J. Ferrera, and H.I. Smith. "Coherence and Structural Design of Free-Standing Gratings for Atom-Wave Optics." Presented at the *MicroProcess Conference*, Sandai, Japan, July 1995. Submitted to *Jap. J. App. Phys.*

Savas, T.A., M.L. Schattenburg, J.M. Carter, and H.I. Smith. "Large-Area Achromatic Interferometric Lithography for 100 nm-Period Gratings and Grids; With Novel Applications." Submitted to *40th International Symposium on Electron Ion and Photon Beam Technology and Nanofabrication.* Symposium on Elect. Ion and Photon Beam Technol. and Nanofab.

Smith, H.I. "A Maskless X-ray Projection Pattern Generator." *40th International Symposium on*

Electron Ion and Photon Beam Technology and Nanofabrication.

Yang, I.Y., D.A. Antoniadis, and H.I. Smith. "Fabrication of Back-gated CMOS Devices Using Mixed and Matched Optical and X-ray Lithographies." Submitted to *40th International Symposium on Electron Ion and Photon Beam Technology and Nanofabrication.*

5.20.3 Theses

Burkhardt, M. "Fabrication Technology and Measurement of Coupled Quantum Dot Devices." Ph.D diss. Dept. of Electr. Eng. and Comput. Sci., MIT, 1995.

Shah, S. "Free-standing 100 nm Period Gratings Produced by Achromatic Holographic Lithography." M.E. thesis. Dept. of Electr. Eng. and Comput. Sci., MIT, 1995.

Wong, V.V. "Fabrication of Distributed Feedback Devices Using X-ray Lithography." Ph.D. diss. Dept. of Electr. Eng. and Comput. Sci., MIT, 1995.

Yasaka, A. "Feasibility Study of Spatial-Phase-Locked Focused-Ion-Beam Lithography." S.M. thesis. Dept. of Mat. Sci. and Eng., MIT, 1995.